



## Tuning mPEG-PLA/vitamin E-TPGS-based mixed micelles for combined celecoxib/honokiol therapy for breast cancer



Jiahui Sun<sup>a</sup>, Jing Li<sup>b</sup>, Qi Liu<sup>c</sup>, Min Jiang<sup>a</sup>, Mengjia Yang<sup>a</sup>, Siwen Zhan<sup>a</sup>, Tong Qiu<sup>d</sup>, Kaiyong He<sup>e,\*</sup>, Xueqiong Zhang<sup>a,\*</sup>

<sup>a</sup> Department of Pharmaceutical Engineering, School of Chemical Engineering, Wuhan University of Technology, Wuhan 430070, PR China

<sup>b</sup> State Key Laboratory of Advanced Technology for Materials Synthesis and Processing, Wuhan University of Technology, Wuhan 430070, PR China

<sup>c</sup> Department of Dermatology, Johns Hopkins University School of Medicine, Baltimore, Maryland, 21231, USA

<sup>d</sup> Biomedical Materials and Engineering Center, Wuhan University of Technology, Wuhan 430070, PR China

<sup>e</sup> Hubei Institute for Drug Control, Wuhan 430070, PR China

### ARTICLE INFO

#### Keywords:

Breast cancer  
Celecoxib  
Honokiol  
Mixed micelles  
Combined treatment  
Synergistic effect

### ABSTRACT

This study aimed to develop, evaluate, and optimize the mPEG-PLA/vitamin E-TPGS mixed micelle drug delivery system to encapsulate celecoxib (CXB) and honokiol (HNK) for intravenous treatment of breast cancer. To this end, we formulated CXB-loaded mPEG-PLA/vitamin E-TPGS (PV-CXB) and HNK-loaded mPEG-PLA/vitamin E-TPGS (PV-HNK) mixed micelles and analyzed their characteristics. The 4T1 cell line was used for cytotoxicity determination and cellular uptake experiments, and for establishing a 4T1-bearing mouse model for histopathology, immunofluorescence, terminal deoxynucleotidyl transferase-mediated nick end labeling, and Western blot analysis. The synergistic effects of PV-CXB and PV-HNK combination therapy were investigated in vitro and in vivo using the coefficient of drug interaction values. The mean size of PV-CXB and PV-HNK prepared with optimal formulation was approximately 50 nm, with a spherical shape. PV-CXB and PV-HNK combination therapy exhibited cytotoxicity in 4T1 cells in vitro. However, the toxicity of PV-CXB and PV-HNK combination therapy was not apparent in normal tissues (heart, liver, spleen, lung, and kidney) in vivo and reduced the expression of collagen fibers in tumor tissues. Moreover, the combination therapy reduced the expression of tumor growth biomarkers (Foxp3, CD4, Gr-1, CD11b, CD31, Ki67, FoxM1, and VEGF). In addition, the tumor cell apoptosis rate reached  $45.71 \pm 0.62\%$ . The combined treatment with PV-CXB and PV-HNK showed synergistic effect both in vitro and in vivo. Thus, the PV-CXB and PV-HNK drug delivery system could be used as a potential combination therapy for breast cancer.

### 1. Introduction

Breast cancer is the most frequently diagnosed cancer and the primary cause of cancer-related deaths in women (Bray et al., 2018). At present, the primary treatments for cancer are surgery, radiotherapy, and chemotherapy. Of these, chemotherapy is most widely used for cancer treatment (Lai et al., 2012; Peer et al., 2007). These methods usually kill healthy cells and are toxic to patients. The main obstacles in the successful treatment of cancer are the obvious adverse effects of chemotherapy, such as digestive tract adverse reactions, myelosuppression, hair loss, and multi-drug resistance (MDR) (Jeswani et al., 2018; Yang et al., 2012; Peer et al., 2007).

To help reduce and overcome drug resistance, combination chemotherapy has been clinically used as a cancer treatment for an overall

improved antitumor treatment outcome (El-Far et al., 2018; Sabra et al., 2018; Glasgow and Chougule, 2015). Unlike monotherapy, combination therapy can produce synergistic, additive, and antagonistic effects; therefore, it is necessary to modulate the concentration of two drugs to produce synergistic effects, maximizing therapeutic effects to overcome drug resistance (Tang et al., 2015; Hu and Zhang, 2012).

Nanotechnology is an advisable approach in the treatment of cancer (Peer et al., 2007). By reaching the tumor sites via passive or active targeted administration, enhancing drug efficacy, and reducing drug side effects, nanotechnology provides broad application prospects for cancer research and nanomedicine (Davis et al., 2008; Peer et al., 2007). Accordingly, nanoparticles are emerging as a drug for cancer treatment (Grobymyer et al., 2011; Davis et al., 2008). Researchers believe that we will soon enter an era of diagnosis and treatment of

\* Corresponding authors.

E-mail addresses: [13971376736@163.com](mailto:13971376736@163.com) (K. He), [zhangxq@whut.edu.cn](mailto:zhangxq@whut.edu.cn) (X. Zhang).

<https://doi.org/10.1016/j.ejps.2020.105277>

Received 31 August 2019; Received in revised form 13 January 2020; Accepted 21 February 2020

Available online 24 February 2020

0928-0987/ © 2020 Elsevier B.V. All rights reserved.

tumors based on the administration of nanocarriers (Peer et al., 2007).

The nanotechnology-based combination chemotherapy method includes simultaneously encapsulating two drugs in one nanocarrier, which causes the simultaneous drug delivery and release of the two drugs, or separately encapsulating each drug in separate nanocarriers with the two drugs being administered in the desired ratio (Zhao et al., 2018; Krishnamurthy et al., 2015; Zhang et al., 2012; Dicko et al., 2010).

To date, mPEG-PLA, long considered safe, has been widely studied as an intravenous injectable drug nanocarrier, approved for clinical use by the U.S. Food and Drug Administration (FDA) (Danquah et al., 2009; Zhang et al., 2006). Vitamin E-TPGS is an outstanding solubilizer and emulsifier that could enhance the bioavailability of hydrophobic drugs and restrain P-glycoprotein-mediated MDR (Mi et al., 2011). mPEG-PLA and vitamin E-TPGS have been used to prepare mixed micelles to improve the drug bioavailability, ensure stable dilution performance, and increase drug-loading capacity (Yu et al., 2017; Huang et al., 2014b).

Additionally, many natural compounds mainly derived from Chinese herbal medicines can inhibit the growth and development of cancer (Huang et al., 2016). The chemical components in these natural compounds include phenols and polyphenols, flavonoids, terpenes, organic acids, alkaloids, ketosteroid, and mineral salt, such as artemisinin (a terpene isolated from *Artemisia annua L*), berberine (an alkaloid isolated from *Coptidis rhizome*), and paeonol (a phenol isolated from the root bark of *Peonia moutan*) (Huang et al., 2016; Hsiao and Liu, 2010).

Traditional Chinese medicine (CM) and modern Western medicine (WM) complement each other; therefore, integrative medicine therapy might be a reasonable method to treat cancer (Tang et al., 2012). CM has the advantages of low cost, low toxicity, effective targeting, and MDR reversion (Li et al., 2014). The combination of CM and WM for the treatment of cancer has the potential to relieve symptoms, reverse immunosuppression, reduce metastasis, reduce side effects, and prolong the survival of patients with cancer (Tang et al., 2016; 2012).

Celecoxib is a specific COX-2 inhibitor that belongs to the group of nonsteroidal anti-inflammatory drugs (NSAIDs) (Joshi and Patravale, 2008), initially approved by the FDA for its oral capsules and marketed by Pfizer Inc. (New York, NY, USA) in 1999. Celecoxib exhibits analgesic, anti-inflammatory, and antipyretic effects and has been clinically used to treat inflammatory diseases, such as rheumatoid arthritis and osteoarthritis (J.Q. Li et al., 2018; Sobolewski et al., 2010). Accumulating

preclinical evidence also suggests that it mediates several potential anti-tumor activities, such as the inhibition of the COX-2 pathway, inhibition of tumor cell proliferation, tumor cell apoptosis induction, tumor micro-environment regulation, angiogenesis arrest, immune function regulation, MDR reversion, and re-sensitization to other antitumor drugs (J.Q. Li et al., 2018; Fantappie et al., 2007). Studies have found that celecoxib is used in patients with advanced cancer for which risks include cardiovascular toxicity, rash, gastrointestinal tract adverse reactions, and anemia but considering that the drug is prescribed to treat life-threatening diseases, these risks are acceptable (J.Q. Li et al., 2018). However, celecoxib has poor water solubility (7  $\mu\text{g}/\text{mL}$ ) (Sendher and Bhatia, 2003), which limits its wide clinical application.

Honokiol, a natural biphenyl (a phenolic compound) extracted from the root bark and branches of Chinese medicinal herb *magnolia* plants, has various pharmacological effects without remarkable toxicity in vivo (Zheng et al., 2010; Munroe et al., 2007). In addition, honokiol has potential antitumor effects, such as inhibition of tumor cell growth, induction of tumor cell apoptosis, induction of tumor cell differentiation, angiogenesis inhibition, tumor metastasis inhibition, and MDR reversion (Hwang and Park, 2010; Wolf et al., 2007; Xu et al., 2006). However, honokiol also has poor water solubility, which restricts its clinical application (Wei et al., 2009).

Combination therapy with celecoxib and honokiol for cancer treatment is expected to have coordinated effects because honokiol inhibits the migration of cancer cells caused by decreased levels of COX-2 and prostaglandin E2, and can also reduce the level of  $\beta$ -catenin (Singh and Katiyar, 2013).

In this study, we propose, for the first time, a mPEG-PLA/vitamin E-TPGS mixed micelle drug delivery system to encapsulate celecoxib and honokiol for intravenous treatment of breast cancer. Firstly, mPEG-PLA/vitamin E-TPGS carrier was self-assembled into micelles, celecoxib and honokiol were respectively encapsulated into hydrophobic cores, and physicochemical characterization was completed. Then, the antitumor activity, including the cytotoxicity and the micelle uptake by 4T1 cells, was assessed in vitro. In addition, an in-depth analysis of the antitumor activity was conducted in vivo; the analysis included histopathology, immunofluorescence, terminal deoxynucleotidyl transferase-mediated nick end labeling (TUNEL), and Western blot analysis. Finally, the coefficient of drug interaction (CDI) values were used to determine whether the

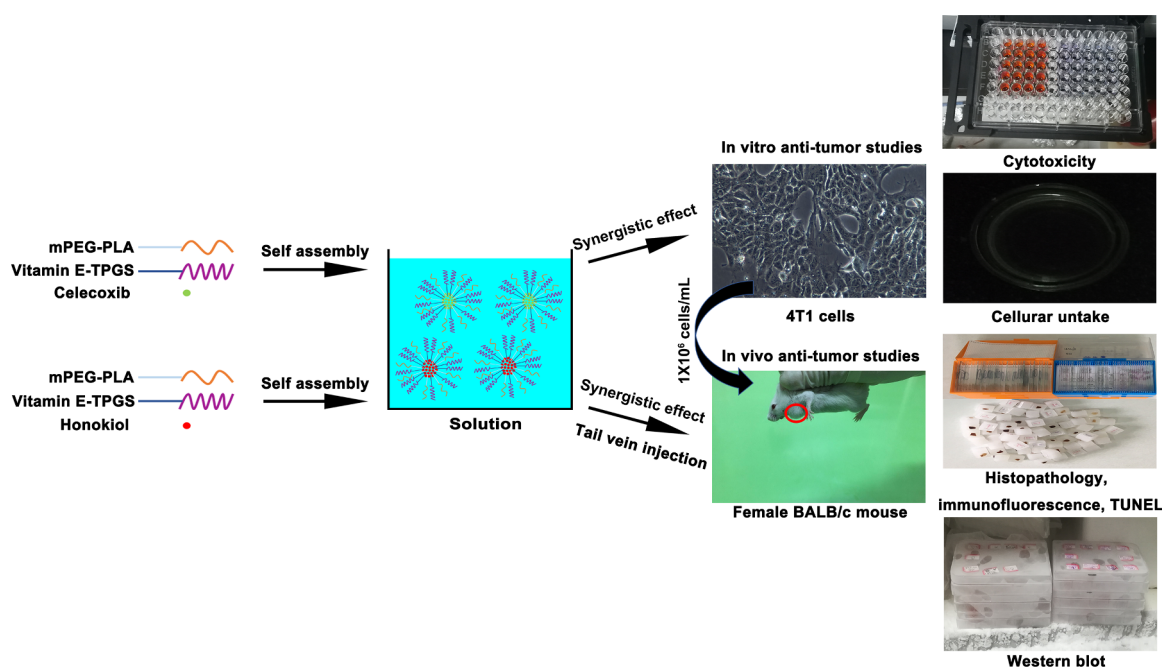


Fig. 1. Schematic illustration of the preparation of PV-CXB and PV-HNK and their antitumor activity in vitro and in vivo.

combined treatment with PV-CXB and PV-HNK has synergistic effects in vitro and in vivo (Fig. 1). The antitumor activities of the combination therapy used here may involve the inhibition of tumor cell proliferation, inhibition of tumor metastasis, inhibition of microvascular growth, reduction of Foxp3<sup>+</sup>CD4<sup>+</sup> regulatory T and Gr-1<sup>+</sup>CD11b<sup>+</sup> myeloid-derived suppressor cell expression in the tumor microenvironment, and the induction of tumor cell apoptosis. The combination of PV-CXB and PV-HNK showed effective synergistic antitumor activity in vitro and in vivo.

## 2. Materials and methods

### 2.1. Materials and cell lines and animals

CXB (≥ 99%) and HNK (≥ 98%) were purchased from Bomei Biotechnology Co., Ltd. (Hefei, China). Monomethoxy-poly (ethylene glycol)-b-poly (D, L-lactide) (mPEG<sub>2000</sub>-PLA<sub>4000</sub>) polymers were purchased from Daigang Biological Technology Co., Ltd. (Jinan, China). D-α-tocopherol polyethylene glycol 1000 succinate (vitamin E-TPGS) was purchased from Aladdin Reagent Co., Ltd. (Shanghai, China). Pyrene (97% purity), Nile red, and fluorescein isothiocyanate (FITC) were obtained from Macklin Biochemical Technology Co., Ltd. (Shanghai, China). RPMI 1640 medium and phosphate buffer saline (PBS) were provided by Suofei Biological Pharmaceutical Technology Co., Ltd. (Shanghai, China). Fetal bovine serum (FBS) was purchased from Zhejiang Tianhang Biotechnology Co., Ltd. (Shaoxing, China). Dimethyl sulfoxide (DMSO), Cell Counting Kit-8 (CCK-8), 4', 6-diamidino-2-phenylindole (DAPI), and 4% neutral paraformaldehyde solution were purchased from Beyotime Biotechnology Co., Ltd. (Shanghai, China). Hematoxylin-eosin (H&E) and Masson's trichrome (MT) stains were purchased from Servicebio Technology Co., Ltd. (Wuhan, China). All other reagents and chemicals were of analytical grade.

4T1 cells were purchased from China Center for Type Culture Collection (Wuhan, China).

Female BALB/c mice (7–8 weeks of age), weighing 16 ± 2 g, were of specific pathogen-free grade and purchased from Hubei Experimental Animal Research Center (Wuhan, China). The license number was SCXK (E) 2015–0018. The animal experimental unit was located at the Hubei Institute for Drug Control (Wuhan, China). All animals were kept under pathogen-free conditions for at least 7 days before the experiments, allowing them to adapt to the new environment. All animal experiments were performed in accordance with the requirements of the National Act on Experimental Animals (China) and Hubei Province Laboratory Animal Management Regulations.

### 2.2. Preparation of PV-CXB and PV-HNK

PV-CXB was prepared using the thin film dispersion method. Initially, CXB and 30 mg of polymer material, including mPEG-PLA and vitamin E-TPGS, were dissolved in 4 mL of acetonitrile. Next, the organic solvent was removed by a rotary evaporator to obtain thin films. After the addition of 4 mL of deionized water, the films were magnetically stirred and finally dispersed in a constant-temperature water bath, allowing the self-assembly of mPEG-PLA/vitamin E-TPGS polymer in water to obtain the micelle solution.

The preparation of PV-HNK was similar to the preparation of the above-mentioned PV-CXB. In the preparation, the mean particle size, polydispersity index (PDI), and encapsulation efficiency (EE%) were used as comprehensive indicators to measure preparation quality. The ratio between mPEG-PLA and vitamin E-TPGS, the water bath temperature, and drug dosage were optimized using single-factor experiments, and final optimal formulations were determined.

### 2.3. Characterization of mixed micelles

#### 2.3.1. Drug-loading efficiency, encapsulation efficiency, and precipitated drug

Micelle solution was centrifuged at 12,000 rpm for 5 min to separate the precipitated crystalline drug. Then, the appropriate amount of the supernatant was collected and diluted with acetonitrile. The UV absorbance of the drug was measured by a UV-Vis spectrophotometer (UV-2600, Shimadzu Ltd., Japan). The maximum absorption wavelength ( $\lambda_{max}$ ) of CXB and HNK was 253 nm and 292 nm, respectively, and there was no UV absorption of the mPEG-PLA/vitamin E-TPGS mixed micelles (PV, empty micelles) at  $\lambda_{max}$ .

DL% and EE% were calculated by applying the following formulas (Sabra et al., 2018):

$$DL(\%) = \frac{\text{weight of drug encapsulated in micelles}}{\text{total weight of micelles}} \times 100\% \quad (1)$$

$$EE(\%) = \frac{\text{weight of drug encapsulated in micelles}}{\text{weight of drug initially added}} \times 100\% \quad (2)$$

Freshly prepared PV-CXB and PV-HNK solution was stored at 4 °C for 48 h, and the content of remaining drug in micelle solution was determined by UV analysis. Precipitated drug (PD%) was calculated according to the following formula (Duan et al., 2016):

$$PD(\%) = \frac{\text{weight of drug initially in micelles} - \text{weight of remaining drug in micelles}}{\text{weight of drug initially in micelles}} \times 100\% \quad (3)$$

#### 2.3.2. Particle size, PDI, and zeta potential

A particle size analyzer (Zetasizer Nano series, Malvern Instruments Ltd., U.K.) was used to measure the average particle size, PDI, and zeta potential of micelles by dynamic light scattering (DLS) method (Butt et al., 2012). Each sample was sufficiently dispersed and tested in triplicate at 25 °C, and the change of light intensity in each sample were recorded at a scattering angle of 90 °.

#### 2.3.3. Apparent morphology

Micelle morphology was observed by transmission electron microscopy (TEM) (JEM-1230, JEOL Ltd., Japan) at an accelerating voltage of 100 kV. Specifically, the micelle solution were diluted to 1 mg/mL and dropped a few drops into copper meshes. After evaporated to dryness, a newly prepared 2% (w/v) phosphotungstic acid solution was added for negative-staining (20 s), dried at room temperature, and observed by TEM.

#### 2.3.4. Stability test

Aliquots of drug-loaded micelle solution (medium: water, pH 7.4 PBS, and RPMI 1640 medium containing 10% v/v FBS) were stored in sealed tubes at 4 °C. PDI and the particle size were measured for a week at specified time points.

#### 2.3.5. In vitro drug release behavior

Aliquots of drug-loaded micelle solution (2 mL) were placed in a dialysis bag (molecular weight cutoff: 3.5 kDa), and then incubated in 20 mL of PBS (pH 7.4, pH 6.5, and pH 5) containing 0.1% w/v Tween 80 and heated in a shaking water bath (100 rpm, 37 °C). Acetonitrile was used to dissolve the free drug in PBS (pH 7.4). At predetermined time points (0 h, 0.5 h, 1 h, 2 h, 4 h, 6 h, 8 h, 10 h, 12 h, 24 h, 34 h, 36 h, 48 h, and 72 h), 3 mL of release medium was withdrawn and replaced with equivalent amounts of fresh PBS, and then subjected to UV analysis.

#### 2.3.6. Critical micelle concentration

The critical micelle concentration (CMC) was determined by fluorescence spectroscopy using pyrene as a fluorescence probe (Dou et al.,

2014). The amphiphilic block polymer solution were mixed with pyrene and allowed to stir at room temperature for 24 h. Final pyrene concentration was  $5 \times 10^{-6}$  M. The amphiphilic block polymer concentration in these experiments ranged from 1  $\mu\text{g}/\text{mL}$  to 200  $\mu\text{g}/\text{mL}$  for mPEG-PLA/vitamin E-TPGS (ratio = 4/1). From an approximate perspective, it is a characteristic feature of micellization that the CMC is independent of temperature (Holmberg et al., 2002), so each sample was tested in triplicate at 25 °C. Fluorescence emission spectra were recorded on a fluorescence spectrophotometer (F-7000, Hitachi Ltd., Japan). The excitation wavelength was 329 nm, and fluorescence spectra were recorded between 350 nm and 450 nm. The excitation and emission slit widths were set to 5 nm.

## 2.4. In vitro antitumor tests

### 2.4.1. Cell viability and CDI in vitro assay

4T1 cells (mouse breast cancer cells) were seeded in 96-well culture plates ( $5 \times 10^3$  cells/well) for 24 h and then incubated with the drug-containing serum medium solutions at 37 °C for 24 h or 48 h. DMSO was used to dissolve free drug, and its concentration in the serum medium was maintained at < 0.1%. The old serum medium was replaced with 100  $\mu\text{L}$  of freshly prepared serum medium containing 10% v/v CCK-8. The absorbance at 450 nm was measured using a microplate reader (Multiskan GO, Thermo Fisher Scientific, US). Each sample was tested in sextuple.

Percent cell viability and CDI were calculated according to the following formula (Zhang et al., 2017; Cao and Zhen, 1989; Damon and Cadman, 1986):

$$\text{Cell Viability}(\%) = (\text{Abs}_{\text{sample}} - \text{Abs}_{\text{blank}}) / (\text{Abs}_{\text{control}} - \text{Abs}_{\text{blank}}) \times 100\% \quad (4)$$

$$\text{CDI} = S_{A+B} / (S_A \times S_B) \times 100 \quad (5)$$

where  $\text{Abs}_{\text{sample}}$  refers to the absorbance of drug prescription groups at different concentrations, while  $\text{Abs}_{\text{blank}}$  refers to the absorbance of the blank group (only serum medium solutions, without cells and drugs), and  $\text{Abs}_{\text{control}}$  refers to the absorbance of the control group (with serum medium solutions, cells without drugs). Here,  $S_{A+B}$ ,  $S_A$ , and  $S_B$  represent the cell viability (%) of sample cells after exposure to both Drug A and Drug B in combination, Drug A, and Drug B relative to control cells, respectively, where CDI values of < 1, > 1, and  $\sim 1$  were considered to exhibit synergistic (+ +), antagonistic (-), and additive (+) effects, respectively.

### 2.4.2. Cellular uptake assay

Micelles containing Nile red and celecoxib and those containing both FITC and honokiol were prepared. The two micelles were dispersed in a serum medium and sonicated at 100 W for 1 min in an ice water bath to form a micelle suspension. 4T1 cells were seeded overnight in a 20 mm laser confocal culture dish ( $1 \times 10^5$  cells/mL) containing 2 mL of serum medium, which was then replaced with the above micelle suspension. The suspension was adjusted to final mass concentrations of 5  $\mu\text{g}/\text{mL}$  of Nile red and 20  $\mu\text{g}/\text{mL}$  of FITC. After incubating for 1 h and 4 h, the medium was removed, and cells were washed with cold PBS. Subsequently, the cells were fixed with 4% neutral paraformaldehyde solution, dyed with DAPI, and finally observed using a confocal laser scanning microscope (CLSM) (TCS SP8, Leica Ltd., Germany).

## 2.5. In vivo antitumor tests

### 2.5.1. Establishment of a 4T1-bearing mouse model

4T1 cells were diluted in PBS (pH = 7.4) to  $1 \times 10^6$  cells/mL. 4T1 tumor cells (200  $\mu\text{L}$ ) were injected into the left side of the mammary fat pad of BALB/c female mice.

### 2.5.2. Dosing regimen

When the tumor volume reached approximately 50  $\text{mm}^3$ , mice were randomly separated into seven groups (five mice per group). The groups included positive control (infected with 4T1 cells but untreated and injected with a stroke-physiological saline solution containing 30% v/v PEG-400), only CXB, only HNK, combined CXB-HNK solution, PV-CXB, PV-HNK, and combined PV-CXB and PV-HNK solution groups.

Drugs from each group were dissolved in a stroke-physiological saline solution containing 30% v/v PEG-400. The tumor-bearing mice were intravenously injected free drugs or drug-loaded micelles equivalent to 5 mg/kg CXB and 3.5 mg/kg HNK (pre-experiment data revealed that this dose can better inhibit tumor growth) three times weekly, for 3 weeks.

Because mPEG-PLA and vitamin E-TPGS have good biocompatibility, they are used as safe adjuvants by the FDA and are widely used in drug delivery systems. Moreover, research has shown that the mPEG-PLA/vitamin E-TPGS mixed micelle system is target-specific and can improve the bioavailability of drugs (Yang et al., 2018; Yu et al., 2017; Huang et al., 2014b; Oh, 2011). Therefore, no empty micelle group was set for in vivo antitumor experiments.

### 2.5.3. In vivo antitumor effect and systemic toxicity evaluation

#### (1) Tumor volume

Tumor volume was calculated using the following formula (Chen et al., 2013):

$$V = (W^2 \times L) / 2 \quad (6)$$

where V is the tumor volume, W is the widest part of the tumor, and L is the lengthiest part of the tumor.

#### (2) Mouse body weight

Mice were weighed to examine the systemic toxicity of the drug.

#### (3) Volume and weight of the isolated tumor

After the last treatment dose (intravenous injectable, 22 days later), all surviving animals were euthanized by cervical dislocation. The isolated tumors were weighed and photographed. The volume of the isolated tumors was calculated according to Eq. (6). Percent tumor growth inhibition (TGI%) was calculated according to the following formula:

$$\text{TGI}(\%) = (W_{\text{control}} - W_{\text{sample}}) / W_{\text{control}} \times 100\% \quad (7)$$

where,  $W_{\text{control}}$  refers to the weight of the isolated tumor of the positive control group,  $W_{\text{sample}}$  refers to the weight of the isolated tumor of the drug prescription groups (only CXB, only HNK, combined CXB-HNK solution, PV-CXB, PV-HNK, and combined PV-CXB and PV-HNK solution).

#### (4) CDI in vivo analysis

The CDI was calculated according to the following formula (Cao and Zhen, 1989; Damon and Cadman, 1986):

$$\text{CDI} = E_{A+B} / (E_A \times E_B) \times 100 \quad (8)$$

where,  $E_{A+B}$ ,  $E_A$ , and  $E_B$  are the percent tumor weights after exposure to both Drug A and Drug B in combination, Drug A, and Drug B relative to the positive control mouse, respectively, where CDI values of < 1, > 1, and  $\sim 1$  were considered to exhibit synergistic (+ +), antagonistic (-), and additive (+) effects.

#### (5) Histopathology, immunofluorescence, and apoptosis analyses

All isolated tissues (heart, liver, spleen, lung, and kidney) and tumors from mice were fixed in 4% neutral paraformaldehyde solution and embedded in paraffin blocks. Subsequently, sections were prepared for H&E staining of mouse tissues and MT staining of isolated tumors. The tumor growth biomarkers (Foxp3, CD4, Gr-1, CD11b, CD31, and Ki67) were determined according to their fluorescence intensity by immunofluorescence-stained sections. The tumor cell apoptosis index was determined based on the TUNEL-stained sections, and an inverted microscope (ECLIPSE TI-SR, Nikon Ltd., Japan) was used to analyze and photograph the sections.

#### (6) Western blot

The excised tumors were divided into two parts: one part was used for the histopathology, immunofluorescence, and apoptosis analyses, as previously described; the other part was homogenized with PBS, and aliquots were stored at  $-80^{\circ}\text{C}$ . The expression of tumor growth biomarkers (FoxM1 and VEGF) was analyzed by Western blot.

#### 2.6. Statistical analysis

All data were expressed as mean  $\pm$  standard error (SD). Statistical analyses were performed using Student's *t*-test or one-way analysis of variance (ANOVA). *p* values less than 0.05 were considered statistically significant. ImageJ software was used for positive expression analysis of the captured images.

### 3. Results and discussion

#### 3.1. Investigation of preparation factors

##### 3.1.1. Water bath temperature

The changes in particle size, PDI, and EE of the obtained product were investigated at  $20^{\circ}\text{C}$ ,  $25^{\circ}\text{C}$ ,  $30^{\circ}\text{C}$ , and  $35^{\circ}\text{C}$ . A total of 30 mg of mixed-micelle carriers was used; the ratio of mPEG<sub>2000</sub>-PLA<sub>4000</sub> to vitamin E-TPGS was 4:1, and the dose was 6 mg. At high temperatures, the particle sizes and the PDI value increased, but the encapsulation efficiency decreased. At  $25^{\circ}\text{C}$ , the encapsulation efficiency was the highest, and the particle size and dispersion were best. The excessive temperature was unfavorable for the construction of the drug-loaded micelle system. This may result from the fact that as temperature increases, the collision between molecules and particles becomes more frequent, which leads to agglomeration and instability of the micelle solution, thus further reducing encapsulation efficiency and drug-loading efficiency, and also increasing particle size (Duan et al., 2016). To efficiently prepare and meet the storage conditions, the hydration temperature was controlled at  $25^{\circ}\text{C}$ .

##### 3.1.2. The ratio of mPEG<sub>2000</sub>-PLA<sub>4000</sub> to vitamin E-TPGS

mPEG<sub>2000</sub>-PLA<sub>4000</sub> and vitamin E-TPGS were selected as carriers, the ratios of mPEG<sub>2000</sub>-PLA<sub>4000</sub> to vitamin E-TPGS were 1:1, 2:1, and 4:1, and the particle size, PDI and encapsulation efficiency of the obtained products were investigated. Thirty milligrams of mPEG<sub>2000</sub>-PLA<sub>4000</sub> and vitamin E-TPGS was used; the dose of celecoxib was 1.8 mg and the dose of honokiol was 3 mg, and the water bath temperature was  $25^{\circ}\text{C}$ . With increasing mass fraction of vitamin E-TPGS in the carrier material, the particle size decreased, but the PDI value and the encapsulation efficiency increased, although the effect was not statistically significant. The CMC value of vitamin E-TPGS was about 0.2 mg/mL and was highly unstable after being diluted into the blood (Chen et al., 2011; Sheu et al., 2003). Amphiphilic block polymer mPEG<sub>2000</sub>-PLA<sub>4000</sub> has a long hydrophobic segment (66.67% of the total molecular weight), and vitamin E-TPGS has a long hydrophilic side chain (66% of the total molecular weight) (Wang et al., 2015). Therefore, mPEG<sub>2000</sub>-

PLA<sub>4000</sub> and vitamin E-TPGS were selected as carriers, and the ratio of mPEG<sub>2000</sub>-PLA<sub>4000</sub> to vitamin E-TPGS was set to 4:1, which helped form a stable system and increased the drug-loading capacity. Notably, the ratio of mPEG<sub>2000</sub>-PLA<sub>4000</sub> and vitamin E-TPGS had less effect on the micelle system, in consistent to other previous reports (Yu et al., 2017; Huang et al., 2014b).

##### 3.1.3. Drug dosages

For the 1.8 mg, 3 mg, and 6 mg drug dose, the particle size, PDI, and EE of the obtained product were investigated. Thirty milligrams of mPEG<sub>2000</sub>-PLA<sub>4000</sub> and vitamin E-TPGS were used, the ratio of mPEG<sub>2000</sub>-PLA<sub>4000</sub> to vitamin E-TPGS was 4:1, and the water bath temperature was  $25^{\circ}\text{C}$ . At higher celecoxib doses, the particle size and PDI value both increased, but the encapsulation efficiency decreased. At a honokiol dosage less than 3 mg, a small change in particle size, PDI value, and encapsulation efficiency was observed. However, when the honokiol dosage was above 3 mg, the particle size and PDI value increased significantly, with a significant reduction in encapsulation efficiency. In order to simultaneously have a large drug encapsulation and loading rate, the final dose of the two drugs was set to 3 mg. Excessive drug dosages were also not conducive to the construction of drug-loaded micelle systems. With higher dosage, the particle size of the micelle system would also increase, results in the decrease of encapsulation rate, and poor dispensability of the micelle system.

The above results are shown in Fig. 2.

#### 3.2. Determination of the optimal prescription and apparent morphology

Through a series of single-factor investigation experiments, the final optimal formulation was determined. The preparation method was the same as that described in Section 2.2. A total of 30 mg of mixed-micelle carriers was used, the ratio between mPEG<sub>2000</sub>-PLA<sub>4000</sub> and vitamin E-TPGS was 4:1, the water bath temperature was set to  $25^{\circ}\text{C}$  and the drug (CXB or HNK) dosage was 3 mg. The TEM images of PV, PV-CXB, and PV-HNK revealed particles with a spherical shape and uniform appearance, with good dispersion, and size less than 50 nm (Fig. 3F). In addition, the small black dots in the background in Fig. 3F were speculated that the phosphotungstic acid staining solution may be easily combined with a certain component in the sample, or the local concentration of the phosphotungstic acid staining solution was relatively high thereby causing black spots. Literature has confirmed that small-sized drug-loaded micelles (10–100 nm) can increase the accumulation of tumor tissue through the enhanced permeability and retention (EPR) effect and reduce the reuptake of micelles by the endothelial system, thereby increasing the long circulation time of micelles in the body and increasing the antitumor effect (Misra et al., 2010; Maeda et al., 2009). Therefore, the prepared micelles showed high potential to passively target tumor tissues.

#### 3.3. Physicochemical characterization of micelle solution

The ultraviolet absorption diagram of PV, CXB, and HNK and the established standard curve of drug concentration versus absorbance are shown in Fig. S1.

The particle size, PDI, zeta potential, EE, DL, and PD results of PV, PV-CXB and PV-HNK prepared under optimal conditions are shown in Table 1, whereas the particle size and zeta potential distribution map are shown in Fig. S2.

The PD% of PV-XB and PV-HNK prepared under optimal conditions was  $3.94 \pm 0.34\%$  (precipitated drug, 48 h, 0.12 mg) and  $2.64 \pm 0.12\%$  (precipitated drug, 48 h, 0.08 mg), respectively. The concentrations of celecoxib and honokiol in the micelle solution prepared at the optimum formulation reached  $563.4 \mu\text{g/mL}$  (EE%,  $75.12 \pm 1.70\%$ ) and  $723.5 \mu\text{g/mL}$  (EE%,  $96.47 \pm 1.92\%$ ),

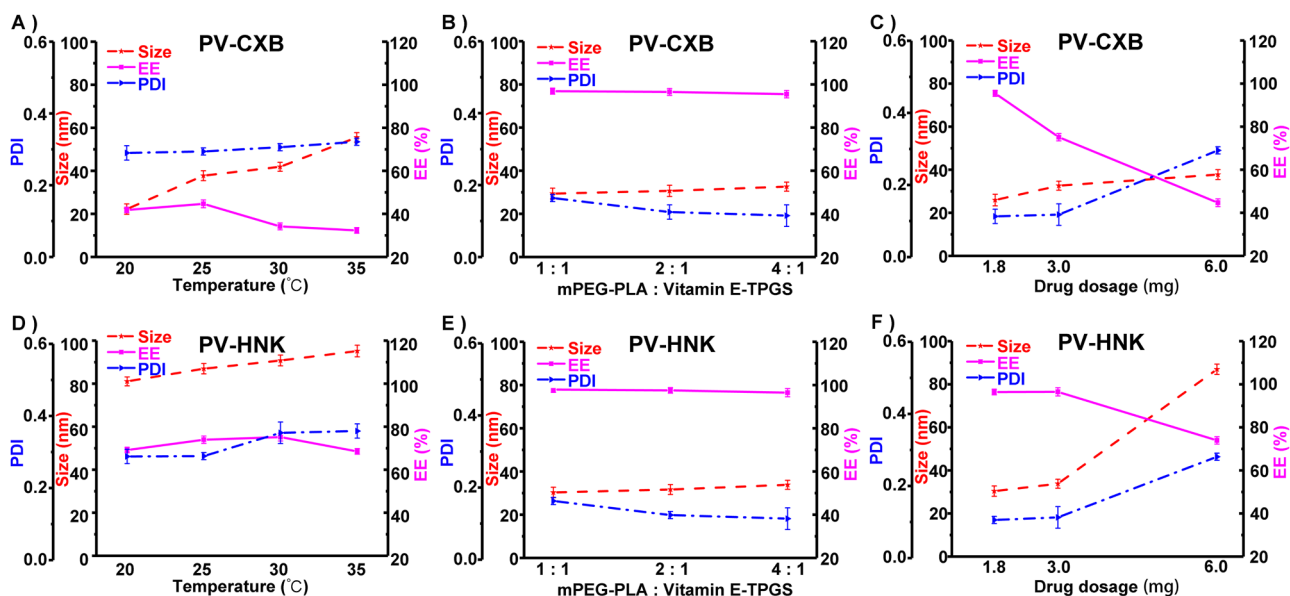


Fig. 2. Effect of preparation factors on the mean particle size, PDI and EE of PV-CXB and PV-HNK. Each value represents the mean  $\pm$  SD ( $n = 3$ ). (A, D) Investigation of water bath temperatures of PV-CXB and PV-HNK. (B, E) Investigation of the ratios of mPEG<sub>2000</sub>-PLA<sub>4000</sub> to vitamin E-TPGS of PV-CXB and PV-HNK. (C, F) Investigation of drug dosages of PV-CXB and PV-HNK.

respectively. Celecoxib and honokiol have poor water solubility (Wei et al., 2009; Sendher and Bhatia, 2003). This indicated that the carrier materials had excellent encapsulation ability, and drug solubility was remarkably improved. It was also worth noting that the zeta potential of micelles in solution was negative, this is consistent with several other reports that the surface charge of PEG-modified nanostructures are also negative (Li et al., 2013; Radovic-Moreno et al., 2012). The negative charge may result from carboxyanion of polylactic acid exposed on the micelle surface (Lee et al., 2007).

### 3.4. Investigation of drug release behavior in vitro

The cumulative release curves of PV-CXB and PV-HNK are shown in Fig. 3A and B.

At pH 7.4, pH 6.5, and pH 5, the cumulative release rates of PV-CXB micelles were 64.71%, 67.89%, and 74.54%, respectively, at 72 h; the cumulative release rates of PV-HNK micelles were 67.21%, 70.30%, and 76.72%, respectively, at 72 h. At pH 7.4, the cumulative release rate of free CXB was 91.37% at 6 h, and the cumulative release rate of free HNK was 98.94% at 6 h. The average extracellular tumor pH is between 6 and 7, while the average in normal tissues and blood is approximately 7.4 (Danhier et al., 2010). At pH 5 and pH 6.5, drug-loaded micelles were released slightly faster than at pH 7.4 at 72 h, which was conducive to the accumulation of drugs in the tumor microenvironment. The original drug was almost completely released in 6 h. Notably, the preparation of the micelles had a specific sustained release effect that can significantly prolong the drug release, but not all encapsulated drugs were released from the micelles. This is also true in many literatures that have shown the cumulative drug release rate of drug-loaded micelles has not reached 100% (Sabra et al., 2018; Yu et al., 2017; Duan et al., 2016; Huang et al., 2014b). The unreleased of all micelles may result from the limitation of drug concentration, micelle degradation rate, and environmental conditions in vitro (Sutton et al., 2007; Liu et al., 2006; Cho et al., 2004; Lavasanifar et al., 2002). In addition, according to the results of literature experiments (Bao et al., 2019), micelle solutions with different drug-loading efficiency have different cumulative drug release rates, and higher drug-loading efficiency will lead to slower drug release rates possibly due to the fact that smaller particle size has larger surface area for drug release; the literature also indicates that the initial burst release is characteristic of the

drug released from the nanoparticle system, this is because as the drug molecules diluted under sinking conditions, they would rapidly dissolve at or near the surface of the nanoparticle.

### 3.5. Investigation of stability and CMC

The stability and CMC of the micelle solution are shown in Fig. 3C-E.

Stability is one of the most important properties of nanocarriers. Nanoparticles used in biomedical fields must be stably dispersed in a certain concentration of salt solution or serum medium (Kim et al., 2010). The mean size and PDI of the two drug-loaded micelle formulations (PV-CXB, PV-HNK; medium: water, pH 7.4 PBS, and RPMI 1640 medium containing 10% v/v FBS) did not change significantly even after 1-week storage under 4 °C, which reflected their excellent stability. The CMC of mixed micelles (5.368  $\mu$ g/mL) was obviously decreased compared with single TPGS micelles (0.2 mg/mL) (Chen et al., 2011; Sheu et al., 2003). Thus, mPEG<sub>2000</sub>-PLA<sub>4000</sub> and vitamin E-TPGS got easier to form micelles and exhibited great resistance to the effect of dilution.

### 3.6. In vitro antitumor activity studies

#### 3.6.1. In vitro toxicity and CDI determination

The viability of 4T1 cells after incubation for 24 h and 48 h with several concentrations of empty micelles, free drug, free double-drug combination, single drug-loaded micelles, and two drug-loaded micelle combination is shown in Fig. 4A-D. Half-maximal inhibitory concentration (IC<sub>50</sub>) values of the drugs are shown in Table 2. CDI in vitro results are shown in Table 3. The results show that both free drugs and drug-loaded micelles significantly inhibited 4T1 cell proliferation in a time- and concentration-dependent manner. The percent cell viability and IC<sub>50</sub> of drug-loaded micelles were significantly lower than those of free-drugs, but the cell inhibition rate of double-loaded micelles was the highest. The cell survival rate of 4T1 cells with empty micelles at the highest concentration (100  $\mu$ g/mL) was still over 80% after incubation for 48 h. This result indicated that mPEG-PLA and vitamin E-TPGS were less cytotoxic and safe, indicating a reliable drug delivery system. The results of CDI showed that different concentrations of PV-CXB and PV-HNK exhibited different degrees of synergy, suggesting that the

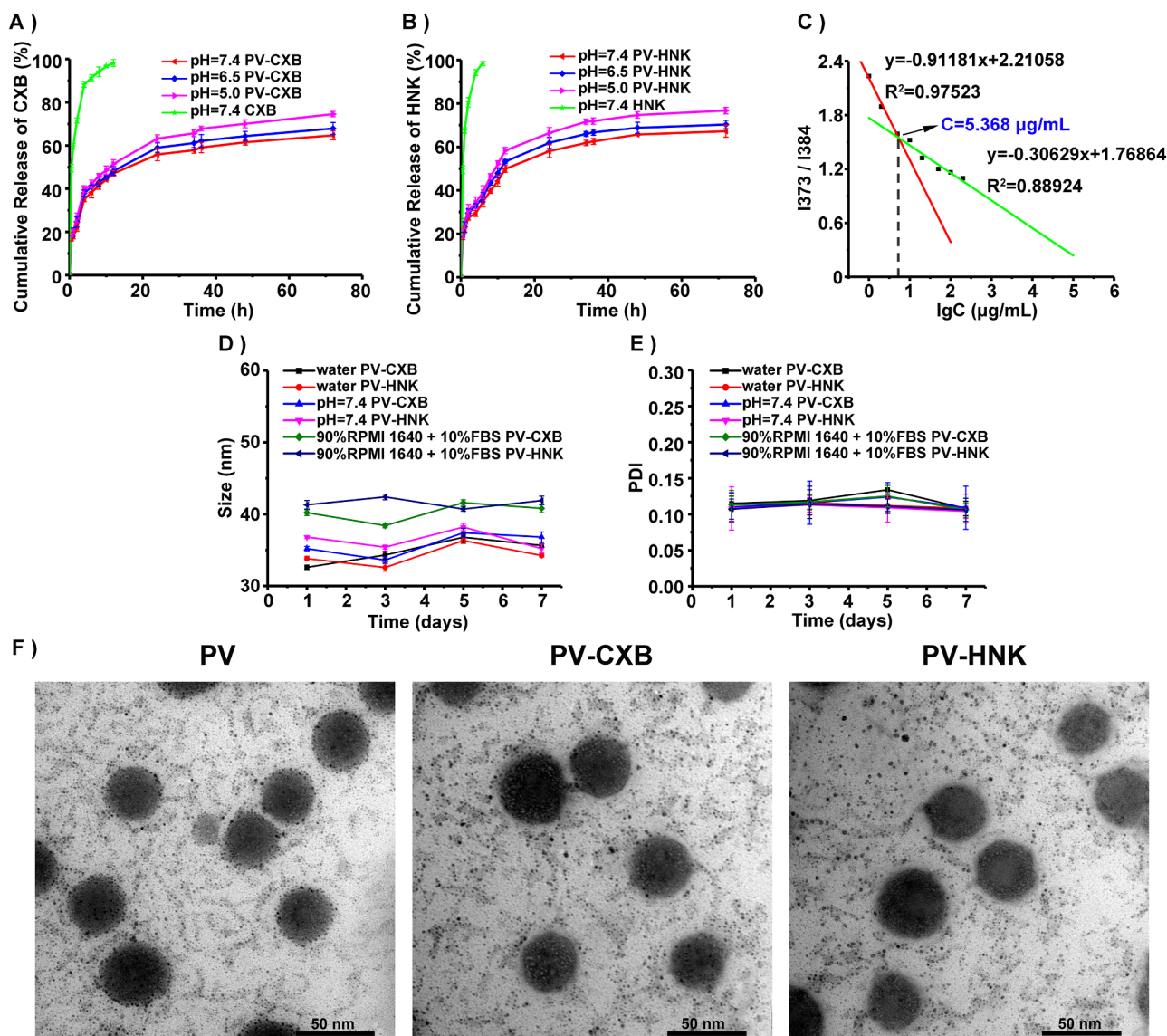


**Fig. 3.** Drug release, CMC characterization, stability, and TEM images of micelles. Each value represents the mean  $\pm$  SD ( $n = 3$ ). (A, B) In vitro cumulative release curves of CXB, PV-CXB, HNK, and PV-HNK at pH 7.4, pH 6.5, and pH 5. (C) CMC of empty mixed micelles. (D, E) Physical stability of drug-loaded micelle solution (medium: water, pH 7.4 PBS and RPMI 1640 medium containing 10% v/v FBS) showing the change in the mean particle size and PDI over time. (F) TEM images of PV, PV-CXB, and PV-HNK. Scale bar: 50 nm.

combination of PV-CXB and PV-HNK reduces the dosage and improves the therapeutic effect at the appropriate dose in vitro.

### 3.6.2. Cellular uptake experiment

Cellular uptake of drug-loaded micelles by 4T1 cells was investigated by a CLSM. The results of 4T1 cells treated with two drug-loaded micelles at 1 h and 4 h are shown in Fig. 4E. After 1 h, the PV-CXB and PV-HNK rapidly accumulated in the cytosol of 4T1 cells, showing bright green and red fluorescence. Brighter fluorescence in the cytosol was observed after 4 h. We observed that both micelles could effectively carry the drug within the cells.

**Table 1**

Physicochemical characteristics of PV, PV-CXB, and PV-HNK. Each value represents the mean  $\pm$  SD ( $n = 3$ ).

Formula	Particle size (nm)	PDI	Zeta potential (mV)	EE (%)	DL (%)	PD (%)
PV	30.97 $\pm$ 1.67	0.106 $\pm$ 0.012	-13.07 $\pm$ 0.12	-	-	-
PV-CXB	32.58 $\pm$ 2.10	0.115 $\pm$ 0.030	-14.20 $\pm$ 0.30	75.12 $\pm$ 1.70%	6.83 $\pm$ 0.31%	3.94 $\pm$ 0.34%
PV-HNK	33.81 $\pm$ 2.30	0.109 $\pm$ 0.024	-13.50 $\pm$ 0.23	96.47 $\pm$ 1.92%	8.77 $\pm$ 0.21%	2.64 $\pm$ 0.12%

### 3.7. In vivo antitumor activity studies

#### 3.7.1. Tumor volume, weight, and mouse body weight

The tumor volume growth curve, mouse body weight curve, and the volume and weight of the isolated tumor are shown in Fig. 5. After 3 weeks of treatment, the average tumor volume and tumor weight of the positive control group reached 1597.72  $\pm$  48.34 mm<sup>3</sup> and 2.51  $\pm$  0.30 g, the PV-HNK group reached 366.32  $\pm$  39.61 mm<sup>3</sup> and 0.96  $\pm$  0.41 g, and the combined PV-CXB and PV-HNK solution group reached 142.74  $\pm$  28.17 mm<sup>3</sup> and 0.35  $\pm$  0.33 g, respectively. In comparison with the positive control group, the tumor volume and tumor weight of all the drug treatment groups decreased significantly

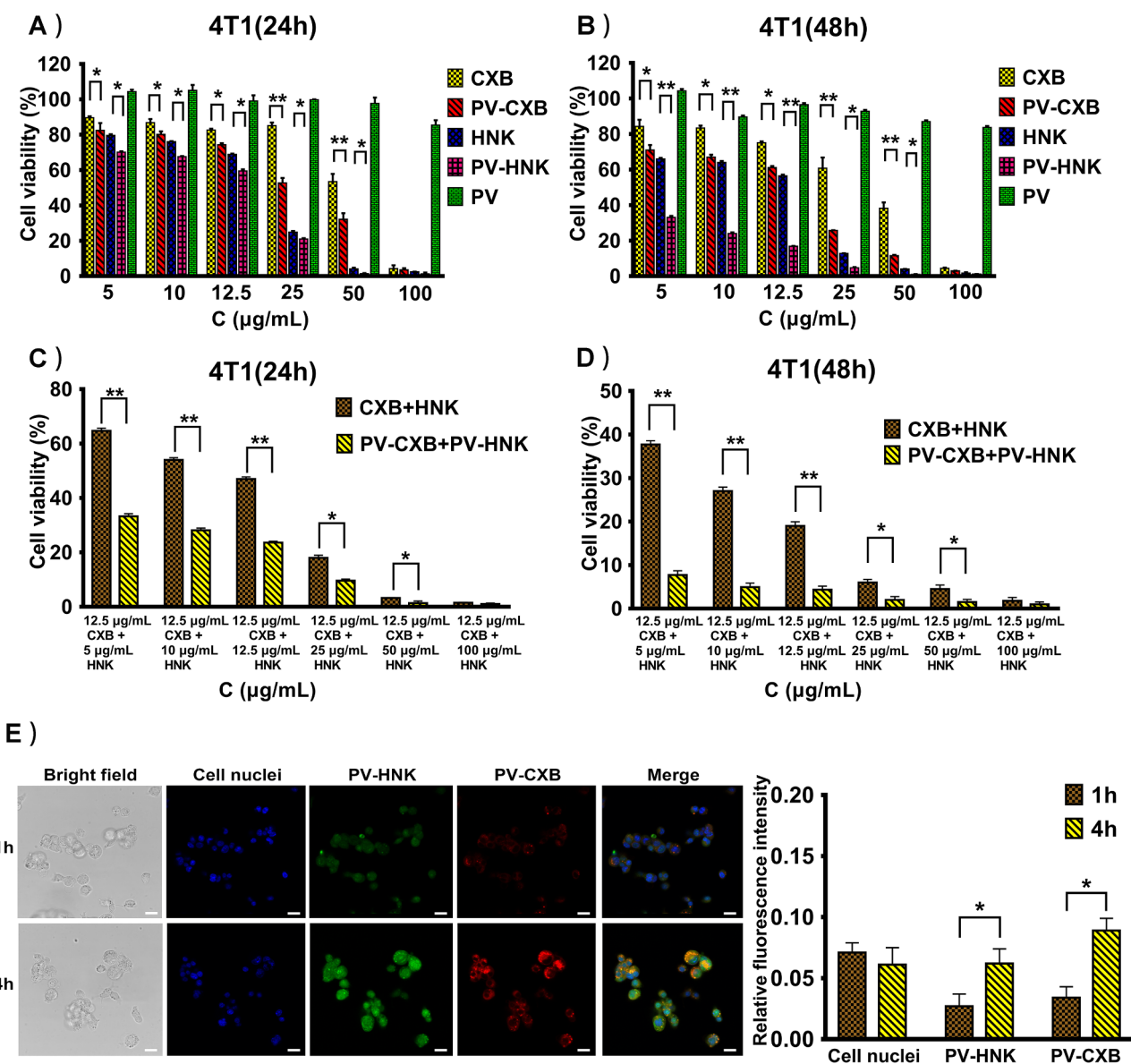


**Fig. 4.** Cytotoxicity study and fluorescence images of 4T1 cells in vitro. Each value represents the mean  $\pm$  SD ( $n = 6$ ). (A, C) The cell viability of empty micelles and different formulations after 24 h of incubation,  $*p < 0.05$ ,  $**p < 0.01$ . (B, D) The cell viability of empty micelles and different formulations after 48 h of incubation,  $*p < 0.05$ ,  $**p < 0.01$ . (E) Fluorescence images and quantitative analysis of 4T1 cells treated with the two drug-loaded micelle combination at different time intervals (1 h and 4 h). In the figure, the blue signal is the cell nuclei stained with DAPI, the red signal is the PV-CXB labeled with Nile red, and the green signal is the PV-HNK labeled with FITC. The two micelles were dispersed in the serum medium and sonicated at 100 W for 1 min in an ice water bath to form micelle suspension. The suspension was adjusted to final mass concentrations of 5  $\mu\text{g/mL}$  of Nile red and 20  $\mu\text{g/mL}$  of FITC. Scale bar: 25  $\mu\text{m}$ . In addition, relative fluorescence intensity means the relative expression of the fluorescence positive density between cell fields. All quantitative calculations were obtained from over eight or more images per group of drug prescriptions for one experiment. Data are presented as mean  $\pm$  SD of three independent experiments,  $*p < 0.05$ .

**Table 2**

IC<sub>50</sub> values of CXB and HNK from different formulations. Each value represents the mean  $\pm$  SD ( $n = 6$ ).

Formula	IC <sub>50</sub> ( $\mu\text{g/mL}$ ; 4T1)	
	24 h	48 h
CXB	47.30 $\pm$ 0.79	29.96 $\pm$ 0.94
PV-CXB	25.53 $\pm$ 0.64 <sup>a</sup>	14.02 $\pm$ 0.79 <sup>a</sup>
HNK	20.62 $\pm$ 0.52	11.66 $\pm$ 0.85
PV-HNK	17.68 $\pm$ 0.98 <sup>b</sup>	4.268 $\pm$ 0.75 <sup>b</sup>

<sup>a</sup>  $p < 0.05$  compared with CXB.

<sup>b</sup>  $p < 0.05$  compared with HNK.

( $p < 0.05$ ). The TGI value of the combined PV-CXB and PV-HNK solution groups reached 86.06%, which was the largest among all groups (Table 4). It was observed that the test drug prescriptions presented

different degrees of anti-breast cancer activity and that the combination of the two drug-loaded micelles had stronger anti-tumor activity. However, there was no significant difference in body weight between the groups during dosing; thus, there was no significant systemic toxicity in each group of drugs.

### 3.7.2. CDI in vivo and TGI analysis

The CDI in vivo and TGI results are shown in Table 4. The CDI values of the combination-free drug group and the combined micelle group were all  $< 1$ , and the CDI value of the combined PV-CXB and PV-HNK solution group (0.66) was smaller than that of the combined CXB and HNK solution group (0.76). This result suggests that the combined dose of these treatments on mice (CXB 5 mg/kg, HNK 3.5 mg/kg) can produce a synergistic effect; thus, the combination of the two micelles

**Table 3**

CDI values in vitro for the combined PV-CXB and PV-HNK solution formulations. Each value represents the mean  $\pm$  SD ( $n = 6$ ).

Concentration ( $\mu\text{g/mL}$ )	Cell viability (%; 4T1; 24 h)	CDI	Cell viability (%; 4T1; 48 h)	CDI
PV-CXB	PV-HNK			
12.5	0	$74.30 \pm 0.92$	-	$61.08 \pm 0.96$
0	5	$70.12 \pm 0.54$	-	$33.06 \pm 0.93$
0	10	$67.53 \pm 0.42$	-	$23.99 \pm 0.65$
0	12.5	$59.52 \pm 0.93$	-	$16.83 \pm 0.26$
0	25	$20.99 \pm 0.52$	-	$4.72 \pm 0.43$
0	50	$2.81 \pm 0.36$	-	$2.39 \pm 0.17$
0	100	$1.72 \pm 0.84$	-	$1.51 \pm 0.02$
12.5	5	$33.29 \pm 0.91$	0.64 (++)	$7.74 \pm 0.97$
12.5	10	$28.09 \pm 0.84$	0.56 (++)	$4.95 \pm 0.93$
12.5	12.5	$23.60 \pm 0.51$	0.53 (++)	$4.35 \pm 0.82$
12.5	25	$9.62 \pm 0.57$	0.62 (++)	$1.99 \pm 0.78$
12.5	50	$1.52 \pm 0.77$	0.73 (++)	$1.05 \pm 0.63$
12.5	100	$1.00 \pm 0.40$	0.78 (++)	$0.65 \pm 0.54$

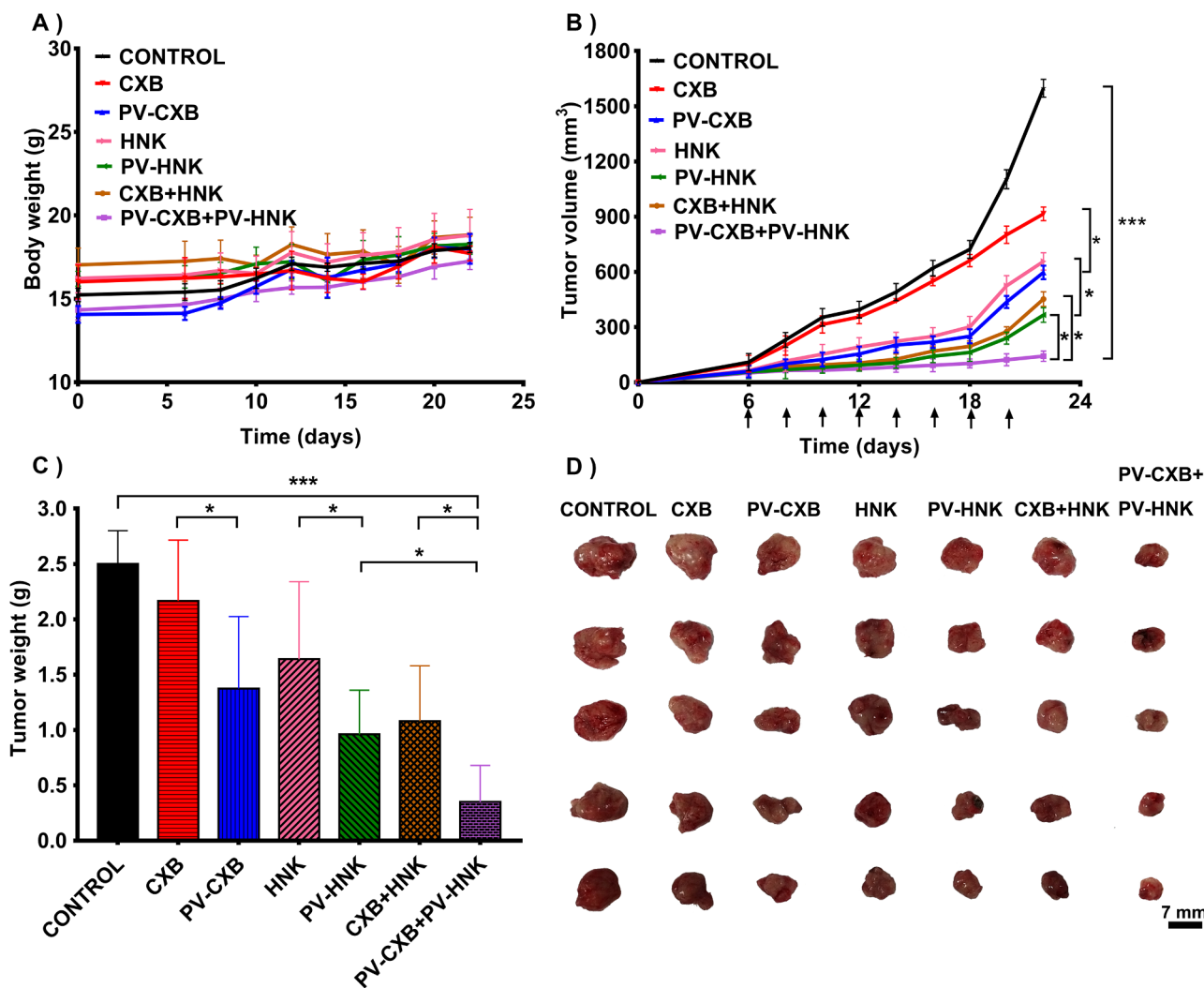


**Fig. 5.** In vivo antitumor efficacy. Establishment of a 4T1-bearing mouse model. The mice received stroke-physiological saline solution containing 30% v/v PEG-400, free CXB, free HNK, free combined CXB-HNK, PV-CXB, PV-HNK, and combined PV-CXB and PV-HNK solution by tail vein injection at a dose of 5 mg/kg for celecoxib and 3.5 mg/kg for honokiol, three times weekly for 3 weeks. Each value represents the mean  $\pm$  SD ( $n = 5$ ). (A) The curves of mouse mass versus time. (B) The growth curve of the tumor volume versus time; predetermined time points of dosing are marked by arrows,  $*p < 0.05$ ,  $***p < 0.001$ . (C) Isolated tumor weight of each group,  $*p < 0.05$ ,  $***p < 0.001$ . (D) Photographs of tumor tissues excised from each group. Scale bar: 7 mm.

has a stronger anti-tumor effect than the combination of the two drugs at this dose.

**3.7.3. H&E staining of mouse tissues**

Clinical use of celecoxib is limited by the severe oral side effects and

cardiovascular problems it cause (J.Q. Li et al., 2018); however, honokiol has no apparent toxicity (Munroe et al., 2007). Histopathological sections of cardiac tissues of mice from the free CXB and free combined CXB-HNK solution groups showed decomposition and dispersion of some cardiomyocytes. However, the mouse body weight of the two

**Table 4**  
CDI in vivo and TGI values for the drug formulations. Each value represents the mean  $\pm$  SD ( $n = 5$ ).

Formula	Tumor weight (g)	TGI (%)	Tumor weight (% of control)	CDI
CONTROL	2.51 $\pm$ 0.30	-	-	-
CXB	2.17 $\pm$ 0.55	13.55	86.45	-
PV-CXB	1.38 $\pm$ 0.65	45.02	54.98	-
HNK	1.64 $\pm$ 0.70	34.66	65.34	-
PV-HNK	0.96 $\pm$ 0.41	61.75	38.25	-
CXB+HNK	1.08 $\pm$ 0.52	56.97	43.03	0.76 (++)
PV-CXB+PV-HNK	0.35 $\pm$ 0.33	86.06	13.94	0.66 (++)

groups did not change significantly, indicating that 5 mg/kg CXB had some side effects on the heart, but no significant systemic toxicity. Interestingly, this side-effect of the micelle group was significantly reduced, and no significant abnormalities were observed in the cell morphology of each organ (Fig. 6). This result may be because the drug was contained within the micelles, which would result in passive targeting. Such targeting would in turn, greatly contribute to the stability of the nano-sized micelles and inhibit the premature release of the drug in the circulatory system.

**3.7.4. Masson's trichrome staining of isolated tumors**

The collagen fibers were stained blue, and the muscle fibers were stained red (Apgar et al., 1998). In the micelle combination group, the number of collagen fibers was small, the majority of tumor cell apoptosis shrank, and cytoplasmic staining deepened. However, this phenomenon was relatively rare in the original drug group. Fig. 6 shows that the number of tumor cells was abundant in the positive control group, with moderate to high abnormality; however, collagen fibers

were simultaneously produced in large quantities (Fig. 8A). Tumor invasiveness is dependent on the degradation of the extracellular matrix (ECM), and collagen fiber is the most critical ECM component. During invasiveness and malignant transformation of tumor cells, the collagen fibers of tumor tissues can affect tumor metastasis by altering the biomechanics of tumors, enzymatic degradation, reorganization, and the distribution of cytokines (Brabrand et al., 2015; Falanga et al., 2002; Yurchenco and Schittny, 1990; Liotta et al., 1980). In fact, patients with collagen-intensive breast tissue have an increased risk of breast cancer (> 4-fold) (Provenzano et al., 2006). These results therefore indicated that the drug prescriptions affected malignant cell proliferation and tumor metastasis to different degrees with the micelle combination group presenting a better antitumor effect.

**3.7.5. Immunofluorescence staining of isolated tumors**

Ki67 marks cells in the proliferative cycle, and the higher the rate of positivity of the marker, the faster the tumor grows (Perez et al., 2015; Dowsett et al., 2011).

The positive expression rate of Ki67 was as follows, from high to low: control (3.46  $\pm$  0.45%), CXB (2.40  $\pm$  0.35%), HNK (1.88  $\pm$  0.14%), PV-CXB (1.05  $\pm$  0.26%), CXB+HNK (0.99  $\pm$  0.30%), PV-HNK (0.58  $\pm$  0.16%), and PV-CXB+PV-HNK (0.10  $\pm$  0.21%).

In tumors, inflammation, and autoimmune diseases, a large number of immature myeloid cells called Gr-1<sup>+</sup>CD11b<sup>+</sup> myeloid-derived suppressor cells (MDSCs) exhibit potent immunosuppressive effects (Ostrand-Rosenberg and Sinha, 2009).

The positive expression rate of Gr-1 plus CD11b was as follows, from high to low: control (40.81  $\pm$  3.20%), CXB (17.31  $\pm$  2.60%), HNK (11.17  $\pm$  0.60%), PV-CXB (8.94  $\pm$  1.21%),

CXB+HNK (6.15  $\pm$  0.62%), PV-HNK (4.72  $\pm$  0.45%), and PV-CXB+PV-HNK (0.33  $\pm$  0.45%).

There is a large amount of Foxp3<sup>+</sup>CD25<sup>+</sup>CD4<sup>+</sup> regulatory T cells

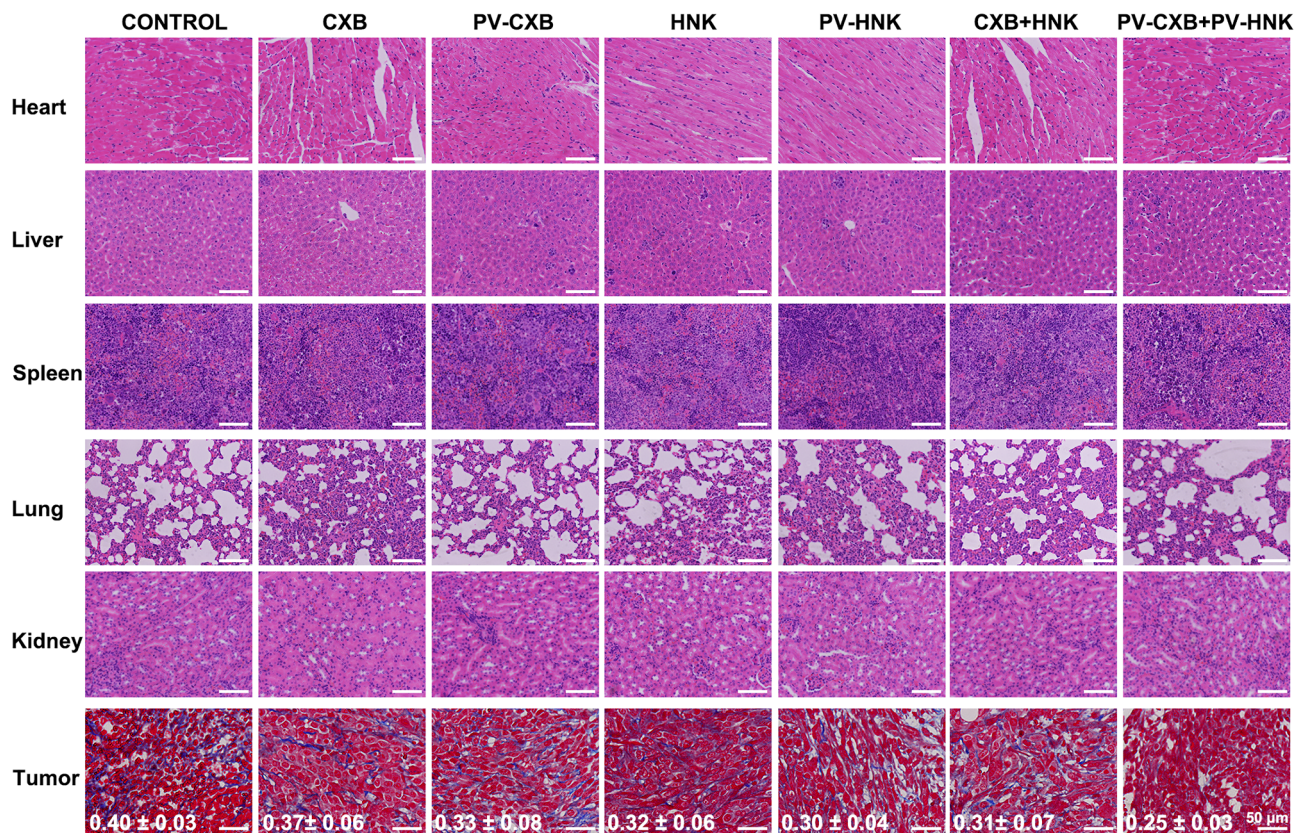


**Fig. 6.** H&E staining of tissues and Masson's trichrome staining of tumor excised from mice under different treatments. All images were captured at 400x magnification. Scale bar: 50  $\mu$ m.

(Tregs) in tumors that are capable of inhibiting a wide range of anti-tumor immune responses. Thus, the consumption of Tregs or the attenuation of their inhibitory function can enhance tumor immunity (Nishikawa and Sakaguchi, 2010).

The positive expression rate of CD4 plus Foxp3 was as follows: control ( $29.29 \pm 1.45\%$ ) > CXB ( $15.03 \pm 1.20\%$ ) > HNK ( $11.88 \pm 1.00\%$ ) > PV-CXB ( $9.60 \pm 1.12\%$ ) >

CXB+HNK ( $6.13 \pm 1.45\%$ ) > (PV-HNK) ( $5.09 \pm 0.96\%$ ) > PV-CXB+PV-HNK ( $0.66 \pm 1.23\%$ ).

CD31 has been used to demonstrate the presence of endothelial cell tissue for assessing tumor angiogenesis, which may reflect the extent of rapidly growing tumors (Sapino et al., 2001).

The positive expression rate of CD31 was as follows: control ( $39.19 \pm 2.21$ ) > CXB ( $23.38 \pm 3.50$ ) > HNK ( $21.44 \pm 1.40$ ) > PV-CXB ( $17.70 \pm 2.60$ ) >

CXB+HNK ( $12.08 \pm 1.31$ ) > PV-HNK ( $10.69 \pm 1.60$ ) > PV-CXB+PV-HNK ( $8.83 \pm 1.59$ ).

The results of CD31 single staining, Ki67 single staining, Gr-1 plus CD11b staining, and CD4 plus Foxp3 staining are shown in Fig. 7A, and those of the quantitative analysis are shown in Fig. 8B, D-F. The results of Ki67, Gr-1 plus CD11b, and CD4 plus Foxp3 staining group were similar to those in the CD31 indicator group, revealing that the drug formulations had different degrees of anti-breast cancer activity (including the combination of the two micelles). Antitumor mechanisms may involve inhibiting malignant cell proliferation, tumor metastasis, and anti-microvascular growth, and attenuating the expression of Foxp3<sup>+</sup>CD4<sup>+</sup>Tregs and Gr-1<sup>+</sup>CD11b<sup>+</sup>MDSCs at tumor tissue sites.

### 3.7.6. TUNEL staining of isolated tumors

TUNEL is the most commonly used method for examining DNA fragmentation (apoptosis) (Majtnerova and Rousar, 2018).

The positive expression rate of TUNEL was observed to be in the following order, from low to high: control ( $1.59 \pm 0.34\%$ ) < CXB ( $8.23 \pm 1.40\%$ ) < HNK ( $12.34 \pm 1.45\%$ ) < PV-CXB ( $18.63 \pm 2.34\%$ ) < CXB+HNK ( $24.76 \pm 1.54\%$ ) < PV-HNK ( $26.24 \pm 1.26\%$ ) < PV-CXB+PV-HNK ( $45.71 \pm 0.62\%$ ).

The results of TUNEL immunofluorescent staining are shown in Fig. 7B, and those of quantitative analyses are shown in Fig. 8C. The highest apoptosis level of the tumor cells was observed in the micelle-combination group ( $45.71 \pm 0.62\%$ ), while apoptotic tumor cells were rarely observed in the positive control group ( $1.59 \pm 0.34\%$ ). These results further supported the anti-breast cancer activity of the drug formulations. The induction of apoptosis in tumor cells was found to be an antitumor mechanism, in addition to the mechanisms previously described in Sections 3.7.4 and 3.7.5.

### 3.7.7. Western blot of isolated tumors

The results of Western blot and quantitative analysis are shown in Fig. 9. VEGF and FoxM1 levels decreased remarkably in the micelle combination group. However, these two proteins showed the highest expression levels in the positive control group.

Most cancer cells produce large amounts of FoxM1 to maintain their rapid growth rate, making FoxM1 one of the most stable tumor biomarkers (C. Huang et al., 2014). FoxM1 affects various aspects of cancer progression, including tumor cell proliferation, tumor angiogenesis, tumor cell invasion, and tumor cell metastasis (Li et al., 2018; Yang et al., 2013). FoxM1 is an important prognostic factor and a promising candidate for breast cancer treatment (Lu et al., 2018).

Tumor cells secrete a protein, VEGF, which stimulates endothelial cell proliferation, promotes angiogenesis, and increases vascular permeability (Carlile et al., 2001). VEGF has also been implicated in tumor angiogenesis, tumor cell proliferation, and tumor cell metastasis (Carlile et al., 2001) and is a crucial biological target for cancer treatment (Carmeliet, 2005).

Therefore, indicating an antitumor mechanism for the drug prescriptions, as shown previously in Sections 3.7.4, 3.7.5, and 3.7.6.

## 4. Conclusions

In this study, two types of drug-loaded micelles were prepared using the membrane hydration method. Average particle size of these drug-loaded micelles was within 50 nm, while the better dispersion and zeta

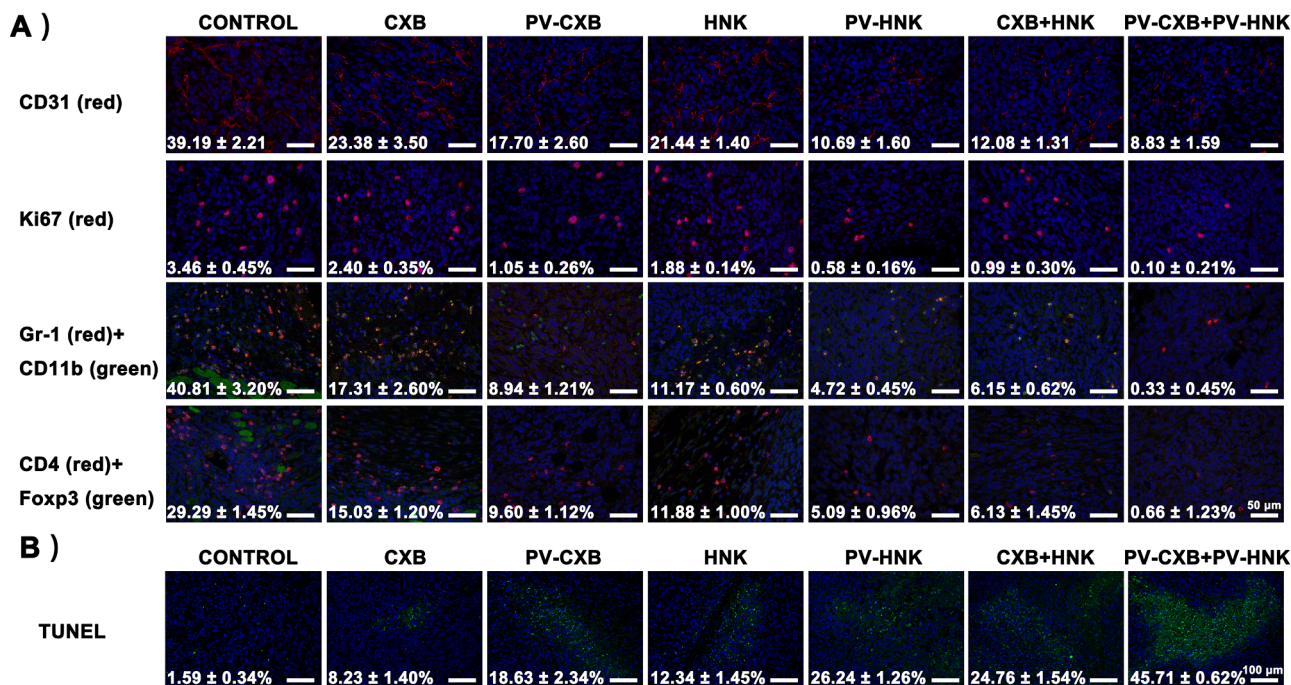
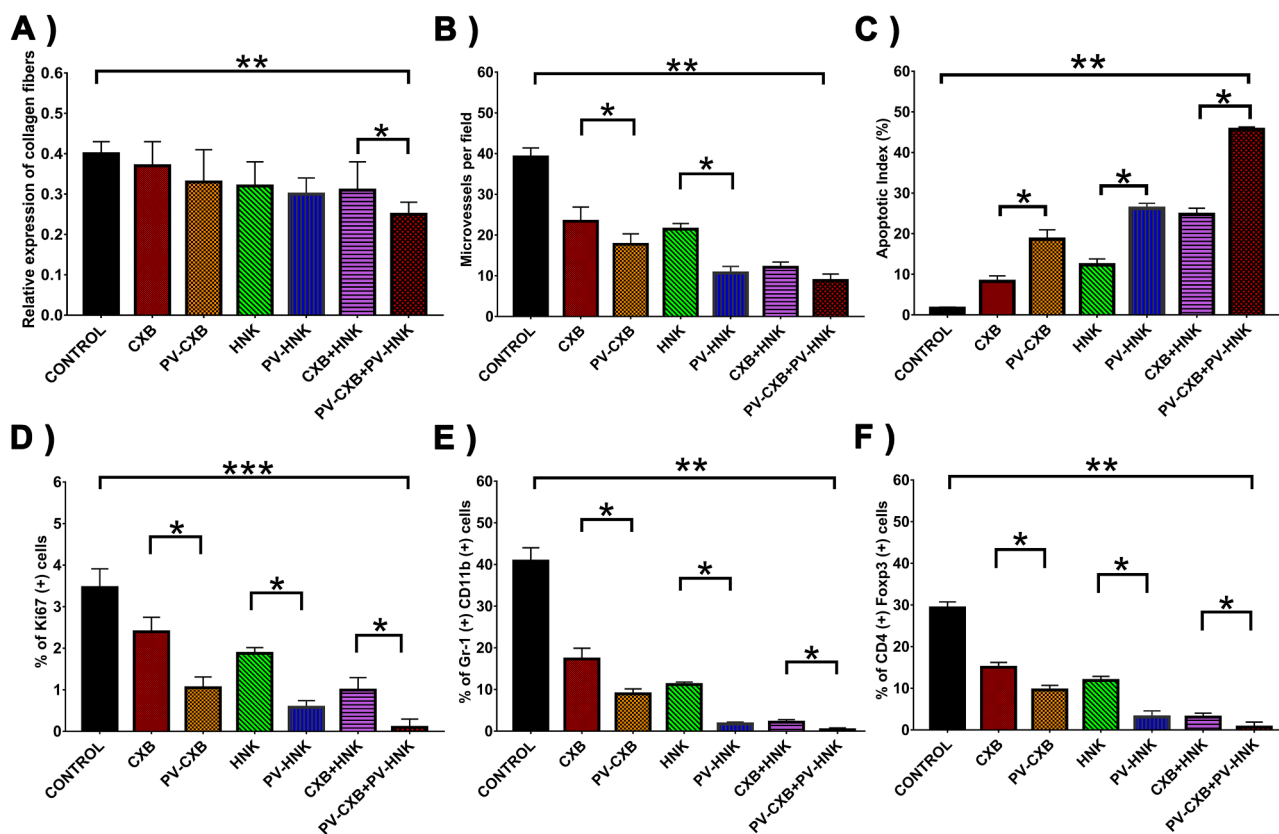
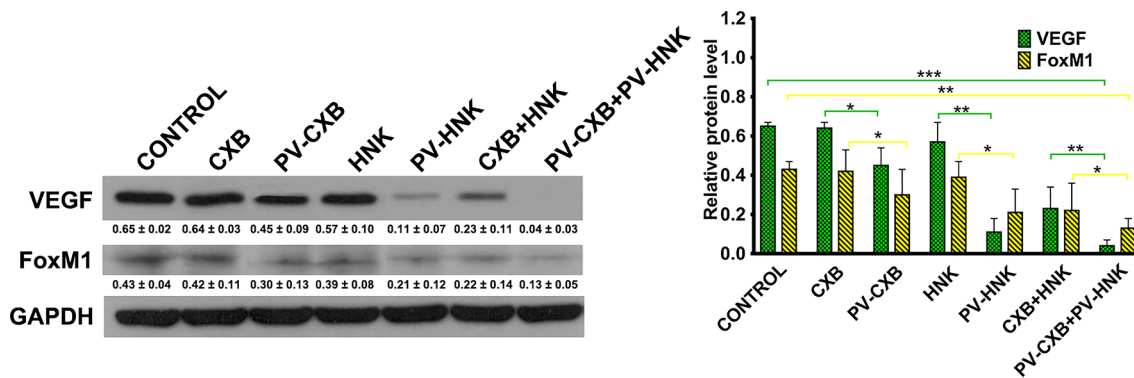


Fig. 7. Immunofluorescence and TUNEL immunofluorescent staining of tumors excised from mice under different treatments. (A) Immunofluorescence images. All images were recorded at 400x magnification. Scale bar: 50  $\mu$ m. In all figures, the blue signal is the cell nuclei stained with DAPI, the red or green signal is the tumor growth biomarkers (Foxp3, CD4, Gr-1, CD11b, CD31, Ki67) stained with fluorescent dye-labeled antibody. (B) TUNEL images. All images were recorded at 200x magnification. Scale bar: 100  $\mu$ m. In the figure, the blue signal is cell nuclei stained with DAPI, and the green signal is the apoptotic cells labeled with FITC.



**Fig. 8.** Masson's trichrome staining, immunofluorescence staining, and TUNEL immunofluorescent staining quantitative analyses. All of the above calculations were obtained from over eight or more images per group of drug prescriptions for one experiment. Data are presented as mean  $\pm$  SD of three independent experiments, \* $p < 0.05$ , \*\* $p < 0.01$ , \*\*\* $p < 0.001$ . (A) The relative expression of the collagen fibers positive density between cell fields. (B) The numbers of microvessels per high-power field. (C-F) The percentage of corresponding biomarker-positive cells among the cells.



**Fig. 9.** Results of Western blotting and quantitative analysis of VEGF & FoxM1 tumor protein levels under different treatments. Relative protein level of each drug prescription group was calculated by comparison with the GAPDH protein levels, unless specifically stated. Data are presented as mean  $\pm$  SD of three independent experiments, \* $p < 0.05$ , \*\* $p < 0.01$ , \*\*\* $p < 0.001$ .

potential values were between  $-13$  mV and  $-15$  mV. Both types of drug-loaded micelles had high drug-loading and encapsulation efficiency. Moreover, TEM images of both types revealed a spherical shape with a uniform particle appearance. Micelle carriers had a low CMC value and could be stored for a week at  $4^\circ\text{C}$ . Drug-loaded micelles had a sustained release effect.

The combination of two micelles had excellent synergistic antitumor activity in vitro and in vivo. There were multiple mechanisms that may play an important role in the antitumor activity. Thus, the combination of CXB-loaded mPEG-PLA/vitamin E-TPGS mixed micelles and the HNK-loaded mPEG-PLA/vitamin E-TPGS mixed micelle drug delivery system has therapeutic potential in breast cancer treatment.

### Declaration of Competing Interest

The authors declare no conflicts of interest.

### Supplementary materials

Supplementary material associated with this article can be found, in the online version, at [doi:10.1016/j.ejps.2020.105277](https://doi.org/10.1016/j.ejps.2020.105277).

### References

Apgar, J.M., Juarranz, A., Espada, J., Villanueva, A., Canete, M., Stockert, J.C., 1998.

- Fluorescence microscopy of rat embryo sections stained with haematoxylin-eosin and masson's trichrome method. *J. Microsc.* 191, 20–27. <https://doi.org/10.1046/j.1365-2818.1998.00348.x>.
- Bao, Z.S., Zhou, Y.F., Lei, L., Zhang, R.S., Song, Q.Q., Li, X.Y., Wang, Y.Q., 2019. A facile strategy to generate high drug payload celecoxib micelles for enhanced corneal permeability. *J. Biomed. Nanotechnol.* 15, 822–829. <https://doi.org/10.1166/jbn.2019.2730>.
- Bray, F., Ferlay, J., Soerjomataram, I., Siegel, R.L., Torre, L.A., Jemal, A., 2018. Global cancer statistics 2018: GLOBOCAN estimates of incidence and mortality worldwide for 36 cancers in 185 countries. *CA-Cancer J. Clin.* 68, 394–424. <https://doi.org/10.3322/caac.21492>.
- Brabrand, A., Kariuki, I.I., Engstrom, M.J., Haugen, O.A., Dyrnes, L.A., Asvold, B.O., Lilledahl, M.B., Bofin, A.M., 2015. Alterations in collagen fibre patterns in breast cancer. A premise for tumour invasiveness? *APMIS* 123, 1–8. <https://doi.org/10.1111/apm.12298>.
- Chen, Y.C., Lo, C.L., Lin, Y.F., Hsiue, G.H., 2013. Rapamycin encapsulated in dual-responsive micelles for cancer therapy. *Biomaterials* 34, 1115–1127. <https://doi.org/10.1016/j.biomaterials.2012.10.034>.
- Carmeliet, P., 2005. VEGF as a key mediator of angiogenesis in cancer. *Oncology* 69, 4–10. <https://doi.org/10.1159/000088478>.
- Chen, W., Miao, Y.Q., Fan, D.J., Yang, S.S., Lin, X., Meng, L.K., Tang, X., 2011. Bioavailability study of berberine and the enhancing effects of TPGS on intestinal absorption in rats. *AAPS PharmSciTech* 12, 705–711. <https://doi.org/10.1208/s12249-011-9632-z>.
- Cho, Y.W., Lee, J., Lee, S.C., Huh, K.M., Park, K., 2004. Hydrotropic agents for study of in vitro paclitaxel release from polymeric micelles. *J. Control. Release* 97, 249–257. <https://doi.org/10.1016/j.jconrel.2004.03.013>.
- Carlisle, J., Harada, K., Baillie, R., Macluskay, M., Chisholm, D.M., Ogdan, G.R., Schor, S.L., Schor, A.M., 2001. Vascular endothelial growth factor (VEGF) expression in oral tissues: possible relevance to angiogenesis, tumour progression and field cancerisation. *J. Oral Pathol. Med.* 30, 449–457. <https://doi.org/10.1034/j.1600-0714.2001.030008449.x>.
- Butt, A.M., Amin, M.C.I.M., Katas, H., Sarisuta, N., Witoonsarisilp, W., Benjakul, R., 2012. In vitro characterization of pluronic F127 and D-alpha-tocopheryl polyethylene glycol 1000 succinate mixed micelles as nanocarriers for targeted anticancer-drug delivery. *J. Nanomater.* 916573. <https://doi.org/10.1155/2012/916573>.
- Cao, S.S., Zhen, Y.S., 1989. Potentiation of antimetabolite antitumor activity in vivo by dipyrindimole and amphotericin B. *Cancer Chemother. Pharmacol.* 24, 181–186. <https://doi.org/10.1007/BF00300240>.
- Dowsett, M., Nielsen, T.O., A'Hern, R., Bartlett, J., Coombes, R.C., Cuzick, J., Ellis, M., Henry, N.L., Hugh, J.C., Lively, T., 2011. Assessment of Ki67 in breast cancer: recommendations from the international Ki67 in breast cancer working group. *J. Natl. Cancer Inst.* 103, 1656–1664. <https://doi.org/10.1093/jnci/djr393>.
- Duan, Y.W., Zhang, B.M., Chu, L.J., Tong, H.H.Y., Liu, W.D., Zhai, G.X., 2016. Evaluation in vitro and in vivo of curcumin-loaded mPEG-PLA/TPGS mixed micelles for oral administration. *Colloid Surf. B-Biointerfaces* 141, 345–354. <https://doi.org/10.1016/j.colsurfb.2016.01.017>.
- Dou, J.F., Zhang, H.Q., Liu, X.J., Zhang, M.Y., Zhai, G.X., 2014. Preparation and evaluation in vitro and in vivo of docetaxel loaded mixed micelles for oral administration. *Colloid Surf. B-Biointerfaces* 114, 20–27. <https://doi.org/10.1016/j.colsurfb.2013.09.010>.
- Dicko, A., Mayer, L.D., Tardi, P.G., 2010. Use of nanoscale delivery systems to maintain synergistic drug ratios in vivo. *Expert Opin. Drug Deliv.* 7, 1329–1341. <https://doi.org/10.1517/17425247.2010.538678>.
- Danhier, F., Feron, O., Preat, V., 2010. To exploit the tumor microenvironment: passive and active tumor targeting of nanocarriers for anti-cancer drug delivery. *J. Control. Release* 148, 135–146. <https://doi.org/10.1016/j.jconrel.2010.08.027>.
- Danquah, M., Li, F., Duke, C.B., Miller, D.D., Mahato, R.I., 2009. Micellar delivery of bicalutamide and embelin for treating prostate cancer. *Pharm. Res.* 26, 2081–2092. <https://doi.org/10.1007/s11095-009-9903-5>.
- Davis, M.E., Chen, Z., Shin, D.M., 2008. Nanoparticle therapeutics: an emerging treatment modality for cancer. *Nat. Rev. Drug Discov.* 7, 771–782. <https://doi.org/10.1038/nrd2614>.
- Damon, L.E., Cadman, M.D., 1986. Advances in rational combination chemotherapy. *Cancer Invest.* 4, 421–444. <https://doi.org/10.3109/07357908609017522>.
- El-Far, S.W., Helmy, M.W., Khattab, S.N., Bekhit, A.A., Hussein, A.A., Elzoghby, A.O., 2018. Phytosomal bilayer-enveloped casein micelles for codelivery of monascus yellow pigments and resveratrol to breast cancer. *Nanomedicine* 13, 481–499. <https://doi.org/10.2217/nmm-2017-0301>.
- Falanga, V., Zhou, L., Yufit, T., 2002. Low oxygen tension stimulates collagen synthesis and COL1A1 transcription through the action of TGF-beta 1. *J. Cell. Physiol.* 191, 42–50. <https://doi.org/10.1002/jcp.10065>.
- Fantappie, O., Solazzo, M., Lasagna, N., Platini, F., Tessitore, L., Mazzanti, R., 2007. P-glycoprotein mediates celecoxib-induced apoptosis in multiple drug-resistant cell lines. *Cancer Res.* 67, 4915–4923. <https://doi.org/10.1158/0008-5472.CAN-06-3952>.
- Glasgow, M.D.K., Chougule, M.B., 2015. Recent developments in active tumor targeted multifunctional nanoparticles for combination chemotherapy in cancer treatment and imaging. *J. Biomed. Nanotechnol.* 11, 1859–1898. <https://doi.org/10.1166/jbn.2015.2145>.
- Grobmyer, S.R., Morse, D.L., Fletcher, B., Gutwein, L.G., Sharma, P., Krishna, V., Frost, S.C., Moudgil, B.M., Brown, S.C., 2011. The promise of nanotechnology for solving clinical problems in breast cancer. *J. Surg. Oncol.* 103, 317–325. <https://doi.org/10.1002/jso.21698>.
- Huang, Z.Y., Huang, Q.J., Ji, L.Y., Wang, Y., Qi, X.X., Liu, L., Liu, Z.Q., Lu, L.L., 2016. Epigenetic regulation of active Chinese herbal components for cancer prevention and treatment: a follow-up review. *Pharmacol. Res.* 114, 1–12. <https://doi.org/10.1016/j.phrs.2016.09.023>.
- Huang, C., Du, J.W., Xie, K.P., 2014a. FOXM1 and its oncogenic signaling in pancreatic cancer pathogenesis. *Biochim. Biophys. Acta-Rev. Cancer* 1845, 104–116. <https://doi.org/10.1016/j.bbcan.2014.01.002>.
- Huang, S.L., Yu, X.H., Yang, L.L., Song, F.L., Chen, G., Lv, Z.F., Li, T., Chen, D., Zhu, W.H., Yu, A.A., Zhang, Y.M., Yang, F., 2014b. The efficacy of nimodipine drug delivery using mPEG-PLA micelles and mPEG-PLA/TPGS mixed micelles. *Eur. J. Pharm. Sci.* 63, 187–198. <https://doi.org/10.1016/j.ejps.2014.07.007>.
- Hu, C.M.J., Zhang, L.F., 2012. Nanoparticle-based combination therapy toward overcoming drug resistance in cancer. *Biochem. Pharmacol.* 83, 1104–1111. <https://doi.org/10.1016/j.bcp.2012.01.008>.
- Holmberg, K., Jönsson, B., Kronberg, B., Lindman, B., 2002. Chapter 2 Surfactant Micellization. *Surfactants and Polymers in Aqueous Solution* 2nd Edition. John Wiley & Sons, Ltd, pp. 39–66. <https://doi.org/10.1002/0470856424.ch2>.
- Hsiao, W.L.W., Liu, L.A., 2010. The role of traditional Chinese herbal medicines in cancer therapy - from TCM theory to mechanistic insights. *Planta Med.* 76, 1118–1131. <https://doi.org/10.1055/s-0030-1250186>.
- Hwang, E.S., Park, K.K., 2010. Magnolol suppresses metastasis via inhibition of invasion, migration, and matrix metalloproteinase-2/-9 activities in PC-3 human prostate carcinoma cells. *Biosci. Biotechnol. Biochem.* 74, 961–967. <https://doi.org/10.1271/bbb.90785>.
- Jeswani, G., Das Paul, S., Jha, A.K., 2018. Advances in the delivery of cancer therapeutics: a comprehensive review. *Curr. Drug Deliv.* 15, 21–36. <https://doi.org/10.2174/1567201814666170726105219>.
- Joshi, M., Patravale, V., 2008. Nanostructured lipid carrier (NLC) based gel of celecoxib. *Int. J. Pharm.* 346, 124–132. <https://doi.org/10.1016/j.ijpharm.2007.05.060>.
- Krishnamurthy, S., Ng, V.W.L., Gao, S.J., Tan, M.H., Hedrick, J.L., Yang, Y.Y., 2015. Codelivery of dual drugs from polymeric micelles for simultaneous targeting of both cancer cells and cancer stem cells. *Nanomedicine* 10, 2819–2832. <https://doi.org/10.2217/nmm.15.109>.
- Kim, S., Shi, Y.Z., Kim, J.Y., Park, K., Cheng, J.X., 2010. Overcoming the barriers in micellar drug delivery: loading efficiency, in vivo stability, and micelle-cell interaction. *Expert Opin. Drug Deliv.* 7, 49–62. <https://doi.org/10.1517/17425240903380446>.
- Li, J.Q., Hao, Q.Y., Cao, W., Vadgama, J.V., Wu, Y., 2018a. Celecoxib in breast cancer prevention and therapy. *Cancer Manag. Res.* 10, 4653–4667. <https://doi.org/10.2147/CMAR.S178567>.
- Lu, X.F., Zheng, D., Liang, W.Q., Chen, C.F., Sun, S.M., Lin, H.Y., 2018. FoxM1 is a promising candidate target in the treatment of breast cancer. *Oncotarget* 9, 842–852. <https://doi.org/10.18632/oncotarget.23182>.
- Li, C., Sun, B.Q., Gai, X.D., 2014. Compounds from Chinese herbal medicines as reversal agents for P-glycoprotein-mediated multidrug resistance in tumours. *Clin. Transl. Oncol.* 16, 593–598. <https://doi.org/10.1007/s12094-014-1169-7>.
- Li, X.X., Ma, K., Song, S.N., Shen, F.Z., Kuang, T., Zhu, Y.Q., Liu, Z.M., 2018. Tight correlation between FoxM1 and FoxP3+ tregs in gastric cancer and their clinical significance. *Clin. Exper. Med.* 18, 413–420. <https://doi.org/10.1007/s12038-018-0505-6>.
- Li, L.Y., Raghupathi, K., Yuan, C.H., Thayumanavan, S., 2013. Surface charge generation in nanogels for activated cellular uptake at tumor-relevant pH. *Chem. Sci.* 4, 3654–3660. <https://doi.org/10.1039/c3sc50899d>.
- Lai, D., Visser-Grieve, S., Yang, X.L., 2012. Tumour suppressor genes in chemotherapeutic drug response. *Biosci. Rep.* 32, 361–374. <https://doi.org/10.1042/BSR20110125>.
- Lee, S.W., Chang, D.H., Shim, M.S., Kim, B.O., Kim, S.O., Seo, M.H., 2007. Ionically fixed polymeric nanoparticles as a novel drug carrier. *Pharm. Res.* 24, 1508–1516. <https://doi.org/10.1007/s11095-007-9269-5>.
- Liu, J., Lee, H., Allen, C., 2006. Formulation of drugs in block copolymer micelles: drug loading and release. *Curr. Pharm. Design* 12, 4685–4701. <https://doi.org/10.2174/138161206779026263>.
- Lavasanifar, A., Samuel, J., Kwon, G.S., 2002. Poly(ethylene oxide)-block-poly(L-amino acid) micelles for drug delivery. *Adv. Drug Deliv. Rev.* 54, 169–190. [https://doi.org/10.1016/S0169-409X\(02\)00115-7](https://doi.org/10.1016/S0169-409X(02)00115-7).
- Liotta, L.A., Tryggvason, K., Garbisa, S., Hart, I., Foltz, C.M., Shafie, S., 1980. Metastatic potential correlates with enzymatic degradation of basement membrane collagen. *Nature* 284, 67–68. <https://doi.org/10.1038/284067a0>.
- Majtnerova, P., Rousar, T., 2018. An overview of apoptosis assays detecting DNA fragmentation. *Mol. Biol. Rep.* 45, 1469–1478. <https://doi.org/10.1007/s11033-018-4258-9>.
- Mi, Y., Liu, Y.T., Feng, S.S., 2011. Formulation of docetaxel by folic acid-conjugated D-alpha-tocopheryl polyethylene glycol succinate 2000 (vitamin E TPGS(2k)) micelles for targeted and synergistic chemotherapy. *Biomaterials* 32, 4058–4066. <https://doi.org/10.1016/j.biomaterials.2011.02.022>.
- Misra, R., Acharya, S., Sahoo, S.K., 2010. Cancer nanotechnology: application of nanotechnology in cancer therapy. *Drug Discov. Today* 15, 842–850. <https://doi.org/10.1016/j.drudis.2010.08.006>.
- Maeda, H., Bharate, G.Y., Daruwalla, J., 2009. Polymeric drugs for efficient tumor-targeted drug delivery based on EPR-effect. *Eur. J. Pharm. Biopharm.* 71, 409–419. <https://doi.org/10.1016/j.ejpb.2008.11.010>.
- Munroe, M.E., Arbiser, J.L., Bishop, G.A., 2007. Honokiol, a natural plant product, inhibits inflammatory signals and alleviates inflammatory arthritis. *J. Immunol.* 179, 753–763. <https://doi.org/10.4049/jimmunol.179.2.753>.
- Nishikawa, H., Sakaguchi, S., 2010. Regulatory T cells in tumor immunity. *Int. J. Cancer* 127, 759–767. <https://doi.org/10.1002/ijc.25429>.
- Oh, J.K., 2011. Poly(lactide) (PLA)-based amphiphilic block copolymers: synthesis, self-assembly, and biomedical applications. *Soft Matter* 7, 5096–5108. <https://doi.org/10.1039/c0sm01539c>.

- Ostrand-Rosenberg, S., Sinha, P., 2009. Myeloid-derived suppressor cells: linking inflammation and cancer. *J. Immunol.* 182, 4499–4506. <https://doi.org/10.4049/jimmunol.0802740>.
- Perez, E., Martinez, A., Teijon, C., Olmo, R., Teijon, J.M., Blanco, M.D., 2015. Improved antitumor effect of paclitaxel administered in vivo as pH and glutathione-sensitive nanohydrogels. *Int. J. Pharm.* 492, 10–19. <https://doi.org/10.1016/j.ijpharm.2015.07.003>.
- Peer, D., Karp, J.M., Hong, S., Farokhzad, O.S., Margalit, R., Langer, R., 2007. Nanocarriers as an emerging platform for cancer therapy. *Nat. Nanotechnol.* 2, 751–760. <https://doi.org/10.1038/nnano.2007.387>.
- Provenzano, P.P., Eliceiri, K.W., Campbell, J.M., Inman, D.R., White, J.G., Keely, P.J., 2006. Collagen reorganization at the tumor-stromal interface facilitates local invasion. *BMC Med.* 4, 38. <https://doi.org/10.1186/1741-7015-4-38>.
- Radovic-Moreno, A.F., Lu, T.K., Puscasu, V.A., Yoon, C.J., Langer, R., Farokhzad, O.C., 2012. Surface charge-switching polymeric nanoparticles for bacterial cell wall-targeted delivery of antibiotics. *ACS Nano* 6, 4279–4287. <https://doi.org/10.1021/nl3008383>.
- Sabra, S.A., Elzoghby, A.O., Sheweita, S.A., Haroun, M., Helmy, M.W., Eldemellawy, M.A., Xia, Y., Goodale, D., Allan, A.L., Rohani, S., 2018. Self-assembled amphiphilic zein-lactoferrin micelles for tumor targeted co-delivery of rapamycin and wogonin to breast cancer. *Eur. J. Pharm. Biopharm.* 128, 156–169. <https://doi.org/10.1016/j.ejpb.2018.04.023>.
- Singh, T., Katiyar, S.K., 2013. Honokiol inhibits non-small cell lung cancer cell migration by targeting PGE<sub>2</sub>-mediated activation of  $\beta$ -catenin signaling. *PLoS One* 8, e06749. <https://doi.org/10.1371/journal.pone.0060749>.
- Sobolewski, C., Cerella, C., Dicato, M., Ghibelli, L., Diederich, M., 2010. The role of cyclooxygenase-2 in cell proliferation and cell death in human malignancies. *Int. J. Cell Biol.* 2010, 215158. <https://doi.org/10.1155/2010/215158>.
- Sutton, D., Nasongkla, N., Blanco, E., Gao, J.M., 2007. Functionalized micellar systems for cancer targeted drug delivery. *Pharm. Res.* 24, 1029–1046. <https://doi.org/10.1007/s11095-006-9223-y>.
- Seedher, N., Bhatia, S., 2003. Solubility enhancement of Cox-2 inhibitors using various solvent systems. *AAPS PharmSciTech* 4, 36–44. <https://doi.org/10.1208/pt040333.E33>.
- Sheu, M.T., Chen, S.Y., Chen, L.C., Ho, H.O., 2003. Influence of micelle solubilization by tocopheryl polyethylene glycol succinate (TPGS) on solubility enhancement and percutaneous penetration of estradiol. *J. Control. Release* 88, 355–368. [https://doi.org/10.1016/S1068-3659\(02\)00492-3](https://doi.org/10.1016/S1068-3659(02)00492-3).
- Sapino, A., Bongiovanni, M., Cassoni, P., Righi, L., Arisio, R., Deaglio, S., Malavasi, F., 2001. Expression of CD31 by cells of extensive ductal in situ and invasive carcinomas of the breast. *J. Pathol.* 194, 254–261. [10.1002/1096-9896\(200106\)194:2<254::AID-PATH880>3.0.CO;2-2](https://doi.org/10.1002/1096-9896(200106)194:2<254::AID-PATH880>3.0.CO;2-2).
- Tang, J., Wennerberg, K., Aittokallio, T., 2015. What is synergy? the Saariselka agreement revisited. *front. Pharmacol.* 6, 181. <https://doi.org/10.3389/fphar.2015.00181>.
- Tang, Z.Y., 2012. Fighting against cancer by integrative medicine. *Chin. J. Integr. Med.* 18, 323–324. <https://doi.org/10.1007/s11655-012-1103-1>.
- Tang, W.R., Yang, S.H., Yu, C.T., Wang, C.C., Huang, S.T., Huang, T.H., Chiang, M.C., Chang, Y.C., 2016. Long-term effectiveness of combined treatment with traditional Chinese medicine and western medicine on the prognosis of patients with lung cancer. *J. Altern. Complement Med.* 22, 212–222. <https://doi.org/10.1089/acm.2015.0214>.
- Wang, J.L., Ma, W.Z., Tu, P.F., 2015. The mechanism of self-assembled mixed micelles in improving curcumin oral absorption: in vitro and in vivo. *Colloid Surf. B-Biointerfaces* 133, 108–119. <https://doi.org/10.1016/j.colsurfb.2015.05.056>.
- Wei, X.W., Gong, C.Y., Shi, S.A., Fu, S.Z., Men, K., Zeng, S., Zheng, X.L., Gou, M.L., Chen, L.J., Qiu, L.Y., Qian, Z.Y., 2009. Self-assembled honokiol-loaded micelles based on poly(epsilon-caprolactone)-poly(ethylene glycol)-poly(epsilon-caprolactone) copolymer. *Int. J. Pharm.* 369, 170–175. <https://doi.org/10.1016/j.ijpharm.2008.10.027>.
- Wolf, I., O'Kelly, J., Wakimoto, N., Nguyen, A., Amblard, F., Karlan, B.Y., Arbiser, J.L., Koeffler, H.P., 2007. Honokiol, a natural biphenyl, inhibits in vitro and in vivo growth of breast cancer through induction of apoptosis and cell cycle arrest. *Int. J. Oncol.* 30, 1529–1537. <https://doi.org/10.3892/ijo.30.6.1529>.
- Yang, C.L., Wu, T.T., Qi, Y., Zhang, Z.P., 2018. Recent advances in the application of vitamin E TPGS for drug delivery. *Theranostics* 8, 464–485. <https://doi.org/10.7150/thno.22711>.
- Xu, D., Lu, Q.H., Hu, X., 2006. Down-regulation of P-glycoprotein expression in MDR breast cancer cell MCF-7/ADR by honokiol. *Cancer Lett.* 243, 274–280. <https://doi.org/10.1016/j.canlet.2005.11.031>.
- Yang, C., Chen, H., Tan, G.X., Gao, W., Cheng, L., Jiang, X., Yu, L., Tan, Y.J., 2013. FOXM1 promotes the epithelial to mesenchymal transition by stimulating the transcription of Slug in human breast cancer. *Cancer Lett.* 340, 104–112. <https://doi.org/10.1016/j.canlet.2013.07.004>.
- Yang, S., Cui, M., Li, H.Y., Zhao, Y.K., Gao, Y.H., Zhu, H.Y., 2012. Meta-analysis of the effectiveness of Chinese and western integrative medicine on medium and advanced lung cancer. *Chin. J. Integr. Med.* 18, 862–867. <https://doi.org/10.1007/s11655-012-1111-1>.
- Yu, A.A., Lv, J.Q., Yuan, F., Xia, Z.H., Fan, K.Y., Chen, G., Ren, J.L., Lin, C.C., Wei, S.J., Yang, F., 2017. mPEG-PLA/TPGS mixed micelles via intranasal administration improved the bioavailability of lamotrigine in the hippocampus. *Int. J. Nanomed.* 12, 8353–8362. <https://doi.org/10.2147/IJN.S145488>.
- Yurchenco, P.D., Schittny, J.C., 1990. Molecular architecture of basement membranes. *Faseb J.* 4, 1577–1590. <https://doi.org/10.1096/fasebj.4.6.2180767>.
- Zhang, Y., Zhang, H., Wang, X.Q., Wang, J.C., Zhang, X., Zhang, Q., 2012. The eradication of breast cancer and cancer stem cells using octreotide modified paclitaxel active targeting micelles and salinomycin passive targeting micelles. *Biomaterials* 33, 679–691. <https://doi.org/10.1016/j.biomaterials.2011.09.072>.
- Zhao, C.Y., Cheng, R., Yang, Z., Tian, Z.M., 2018. Nanotechnology for cancer therapy based on chemotherapy. *Molecules* 23, 826. <https://doi.org/10.3390/molecules23040826>.
- Zheng, X.L., Kan, B., Gou, M.L., Fu, S.Z., Zhang, J., Men, K., Chen, L.J., Luo, F., Zhao, Y.L., Zhao, X., Wei, Y.Q., Qian, Z.Y., 2010. Preparation of mPEG-PLA nanoparticle for honokiol delivery in vitro. *Int. J. Pharm.* 386, 262–267. <https://doi.org/10.1016/j.ijpharm.2009.11.014>.
- Zhang, X.Q., Li, L.H., Li, C.F., Zheng, H., Song, H.Y., Xiong, F.L., Qiu, T., Yang, J., 2017. Cisplatin-crosslinked glutathione-sensitive micelles loaded with doxorubicin for combination and targeted therapy of tumors. *Carbohydr. Polym.* 155, 407–415. <https://doi.org/10.1016/j.carbpol.2016.08.072>.
- Zhang, Q.Z., Zha, L.S., Zhang, Y., Jiang, W.M., Lu, W., Shi, Z.Q., Jiang, X.G., Fu, S.K., 2006. The brain targeting efficiency following nasally applied mPEG-PLA nanoparticles in rats. *J. Drug Target.* 14, 281–290. <https://doi.org/10.1080/10611860600721051>.